



Gem Corundum Deposits of Greece: Geology, Mineralogy and Genesis

Panagiotis Voudouris, Constantinos Mavrogonatos, Ian Graham, Gaston Giuliani, Vasilios Melfos, Stefanos Karampelas, Vilelmini Karantoni, Kandy Wang, Alexandre Tarantola, Khin Zaw, et al.

► To cite this version:

Panagiotis Voudouris, Constantinos Mavrogonatos, Ian Graham, Gaston Giuliani, Vasilios Melfos, et al.. Gem Corundum Deposits of Greece: Geology, Mineralogy and Genesis. Minerals, 2019, 9 (1), pp.49. 10.3390/min9010049 . hal-02932256

HAL Id: hal-02932256

<https://hal.science/hal-02932256>

Submitted on 7 Sep 2020

HAL is a multi-disciplinary open access archive for the deposit and dissemination of scientific research documents, whether they are published or not. The documents may come from teaching and research institutions in France or abroad, or from public or private research centers.







L'archive ouverte pluridisciplinaire **HAL**, est destinée au dépôt et à la diffusion de documents scientifiques de niveau recherche, publiés ou non, émanant des établissements d'enseignement et de recherche français ou étrangers, des laboratoires publics ou privés.



Distributed under a Creative Commons Attribution - NonCommercial - NoDerivatives 4.0 International License

Article

Gem Corundum Deposits of Greece: Geology, Mineralogy and Genesis

Panagiotis Voudouris ^{1,*}, Constantinos Mavrogonatos ¹, Ian Graham ², Gaston Giuliani ³, Vasilios Melfos ⁴, Stefanos Karampelas ⁵, Vilemini Karantoni ⁴, Kandy Wang ², Alexandre Tarantola ⁶, Khin Zaw ⁷, Sebastien Meffre ⁷, Stephan Klemme ⁸, Jasper Berndt ⁸, Stefanie Heidrich ⁹, Federica Zaccarini ¹⁰, Anthony Fallick ¹¹, Maria Tsortanidis ¹ and Andreas Lampridis ¹

¹ Faculty of Geology and Geoenvironment, National and Kapodistrian University of Athens, 15784 Athens, Greece; kmavrogon@geol.uoa.gr (C.M.); m.tsortanidi@hotmail.com (M.T.); andreaslampridis18@gmail.com (A.L.)

² School of Biological, Earth and Environmental Sciences, University of New South Wales, Sydney, NSW 2052, Australia; i.graham@unsw.edu.au (I.G.); kandy.wang@student.unsw.edu.au (K.W.)

³ Université Paul Sabatier, GET/IRD et Université de Lorraine, C.R.P.G./C.N.R.S., 54501 Vandoeuvre, CEDEX, France; giuliani@crpg.cnrs-nancy.fr

⁴ Faculty of Geology, Aristotle University of Thessaloniki, 54124 Thessaloniki, Greece; melfosv@geo.auth.gr (V.M.); wilelminikar@gmail.com (V.K.)

⁵ Bahrain Institute for Pearls & Gemstones (DANAT), WTC East Tower, P.O. Box 17236 Manama, Bahrain; stefanos.karampelas@danat.bh

⁶ UMR GeoResources, Faculté des Sciences et Technologies, Université de Lorraine, 54506 Vandoeuvre-lès-Nancy, France; alexandre.tarantola@univ-lorraine.fr

⁷ CODES Centre of Ore Deposit and Earth Sciences, University of Tasmania, Tas 7001, Australia; khin.zaw@utas.edu.au (K.Z.); sebastien.meffre@utas.edu.au (S.M.)

⁸ Institut für Mineralogie, Westfälische-Wilhelms Universität Münster, 48149 Münster, Germany; stephan.klemme@uni-muenster.de (S.K.); jberndt@uni-muenster.de (J.B.)

⁹ Mineralogisch-Petrographisches Institut, Universität Hamburg, 20146 Hamburg, Germany; stefanie.heidrich@mineralogie.uni-hamburg.de

¹⁰ Department of Applied Geosciences and Geophysics, University of Leoben, 8700 Leoben, Austria; federica.zaccarini@unileoben.ac.at

¹¹ Isotope Geosciences Unit, S.U.E.R.C., Glasgow G75 0QF, UK; anthony.fallick@glasgow.ac.uk

* Correspondence: voudouris@geol.uoa.gr; Tel.: +30-210-727-4129

Received: 13 December 2018; Accepted: 14 January 2019; Published: 15 January 2019



Abstract: Greece contains several gem corundum deposits set within diverse geological settings, mostly within the Rhodope (Xanthi and Drama areas) and Attico-Cycladic (Naxos and Ikaria islands) tectono-metamorphic units. In the Xanthi area, the sapphire (pink, blue to purple) deposits are stratiform, occurring within marble layers alternating with amphibolites. Deep red rubies in the Paranesti-Drama area are restricted to boudinaged lenses of Al-rich metapyroxenites alternating with amphibolites and gneisses. Both occurrences are oriented parallel to the ultra-high pressure/high pressure (UHP/HP) Nestos suture zone. On central Naxos Island, colored sapphires are associated with desilicated granite pegmatites intruding ultramafic lithologies (plumasites), occurring either within the pegmatites themselves or associated metasomatic reaction zones. In contrast, on southern Naxos and Ikaria Islands, blue sapphires occur in extensional fissures within Mesozoic metabauxites hosted in marbles. Mineral inclusions in corundums are in equilibrium and/or postdate corundum crystallization and comprise: spinel and pargasite (Paranesti), spinel, zircon (Xanthi), margarite, zircon, apatite, diaspore, phlogopite and chlorite (Naxos) and chloritoid, ilmenite, hematite, ulvospinel, rutile and zircon (Ikaria). The main chromophore elements within the Greek corundums show a wide range in concentration: the Fe contents vary from (average values) 1099 ppm in the blue sapphires of Xanthi, 424 ppm in the pink sapphires of Xanthi, 2654 ppm for Paranesti rubies, 4326 ppm

for the Ikaria sapphires, 3706 for southern Naxos blue sapphires, 4777 for purple and 3301 for pink sapphire from Naxos plumasite, and finally 4677 to 1532 for blue to colorless sapphires from Naxos plumasites, respectively. The Ti concentrations (average values) are very low in rubies from Paranesti (41 ppm), with values of 2871 ppm and 509 in the blue and pink sapphires of Xanthi, respectively, of 1263 ppm for the Ikaria blue sapphires, and 520 ppm, 181 ppm in Naxos purple, pink sapphires, respectively. The blue to colorless sapphires from Naxos plumasites contain 1944 to 264 ppm Ti, respectively. The very high Ti contents of the Xanthi blue sapphires may reflect submicroscopic rutile inclusions. The Cr (average values) ranges from 4 to 691 ppm in the blue, purple and pink colored corundums from Naxos plumasite, is quite fixed (222 ppm) for Ikaria sapphires, ranges from 90 to 297 ppm in the blue and pink sapphires from Xanthi, reaches 9142 ppm in the corundums of Paranesti, with highest values of 15,347 ppm in deep red colored varieties. Each occurrence has both unique mineral assemblage and trace element chemistry (with variable Fe/Mg, Ga/Mg, Ga/Cr and Fe/Ti ratios). Additionally, oxygen isotope compositions confirm their geological typology, i.e., with, respectively $\delta^{18}\text{O}$ of $4.9 \pm 0.2\text{‰}$ for sapphire in plumasite, 20.5‰ for sapphire in marble and 1‰ for ruby in mafics. The fluid inclusions study evidenced water free CO_2 dominant fluids with traces of CH_4 or N_2 , and low CO_2 densities (0.46 and 0.67 g/cm³), which were probably trapped after the metamorphic peak. The Paranesti, Xanthi and central Naxos corundum deposits can be classified as metamorphic *sensu stricto* (s.s.) and metasomatic, respectively, those from southern Naxos and Ikaria display atypical magmatic signature indicating a hydrothermal origin. Greek corundums are characterized by wide color variation, homogeneity of the color hues, and transparency, and can be considered as potential gemstones.

Keywords: corundum megacrysts; ruby; sapphire; plumasite; metamorphic-metasomatic origin; Greece

1. Introduction

Rubies and sapphires, the two different varieties of the mineral corundum, are among the most popular gemstones used in jewelry. The color in corundum varies from brown, pink to pigeon-blood-red, orange, yellow, green, blue, violet etc. The main chromophore trace elements in corundum are Cr, Fe, Ti and V. Cr^{3+} produces pink and red, while Fe^{2+} – Ti^{4+} pairs produce blue. Distinction of primary gem quality-rubies and sapphires in magmatic and metamorphic is mainly based on the classification schemes presented by Garnier et al. [1], Giuliani et al. [2] and Simonet et al. [3]. Corundum deposits were mainly formed in three periods, the Pan-African orogeny (750–450 Ma), the Himalayan orogeny (45–5 Ma) and the Cenozoic continental rifting with related alkali basalt volcanism (65–1 Ma) [2,4–10]. Magmatic and metamorphic ruby and sapphire deposits related to the Pan-African orogeny are present in southern Madagascar, East Africa, South India and Sri Lanka; those related to the Himalayan orogeny mostly occur in marbles from Central and Southeast Asia. Alkali basalt-related sapphires occur in Australia, northern and central Madagascar, Nigeria, Cameroon, French Massif Central and southeast Asia.

The use of trace element content of gem corundums, in association with their oxygen isotopic signature, is an effective tool in characterizing and interpreting their origin, and can also be used for the exploration, classification and comparison of gem corundum deposits especially those of disputed origin (e.g., placers, xenoliths, etc.) [2,7,11–17].

The presence of corundum in Greece (Xanthi, Naxos and Ikaria islands) has been known of since several years ago, but mostly from unpublished company reports [18–20]. It was only during the 80s, when detailed mineralogical, petrological studies investigated the geological environment of formation for the emery-hosted corundum on Naxos, Samos and Ikaria island [21], and the marble-hosted corundum in Xanthi area [22,23]. Iliopoulos and Katagas [24] described metamorphic

conditions of formation for corundum-bearing metabauxites from Ikaria island. Fieldwork during 1998–2010 by the first two authors resulted in additional findings of corundum megacrysts in Greece, mostly within the Rhodope (Xanthi and Drama areas) and Attico-Cycladic (Naxos and Ikaria islands) tectono-metamorphic units [25–29]. According to these authors, both occurrences in the Rhodope are classified as metamorphic deposits related to meta-limestones (Xanthi deposit) and mafic granulites (Paranesti deposit), based on the scheme of Simonet et al. [3], and supported the theory of their formation during the high temperature-medium pressure retrograde metamorphic episode of carbonates and eclogitic amphibolites during the Cenozoic collision along the Nestos Suture Zone. The plumasite-hosted corundum deposits at Naxos island and those hosted in metabauxites from Ikaria island are classified as metasomatic and metamorphic, respectively [27,29]. Recently, Wang et al. [30] compiled multi-analytical geochemical, mineralogical and petrological studies on rubies from Paranesti Drama area, discussing their origin and comparing the deposit to those in other mafic-ultramafic complexes especially that of Winza in Tanzania.

In addition to the above localities, corundum has been also reported from the Koryfes Hill prospect, which is a telescoped porphyry-epithermal system hosted within Tertiary granitoids in the Kassiteres-Sapes area, on the south of the Rhodope massif (Figure 1). Hydrothermal corundum occurs within a transitional sericitic-sodic/potassic alteration of a quartz-feldspar porphyry, which forms the root zone of an advanced argillic lithocap comprising diaspore, topaz, pyrophyllite and alunite supergroup minerals [31]. Hydrothermal corundum forms up to 3-mm-large aggregates of deep blue-colored crystals that are separated from quartz (and K-feldspar/albite) by a sericite rim. Electron microprobe analyses indicate minor amounts of Fe (up to 0.34 wt. % FeO), Mg (up to 0.02 wt. % MgO) Ti (up to 0.13 wt. % TiO₂) and Cr (up to 0.12 wt. % Cr₂O₃) substituting for Al in the structure. The Koryfes Hill corundum occurrence belongs to those present in porphyry deposits elsewhere and is attributed to the magmatic class of corundum deposits, according to the classification scheme of Simonet et al. [3]. It was suggested by Voudouris [31] that the assemblage corundum-sericite at Koryfes Hill formed as a result of rapid cooling of ascending magmatic-hydrothermal solutions under pressures between 0.6 and 0.3 kb. However, due to its small grain size, which probably rather prevent its use as a gemstone this corundum occurrence will not be further discussed in the present paper.

The aim of this work is to present detailed information on the geology, mineralogy, geochemistry and fluid characteristics involved in the formation of rubies and sapphires in Greece, by expanding on the previous work of the Wang et al. [30], which was only focused on the Paranesti area. New laser ablation inductively coupled plasma mass spectrometry (LA-ICP-MS) and electron probe microanalysis (EPMA) data on corundum will help define their origin and compare them with other famous occurrences elsewhere.

2. Materials and Methods

For this study, the following 18 samples, collected by the first author, were investigated: Naxos samples (Nx1a, Nx1b, Nx2a, Nx2b, Nx3a, Nx3b, Nx4, Nx5a, Nx5b), Ikaria samples (Ik1a, Ik1b), Xanthi samples (Go1a, Go1b, Go5a, Go5b) and Drama samples (Dr1a, Dr1b, Dr2), ranging in color from colorless, to pink, purple, red and blue (Table 1). All occurrences are primary, which is rare for blue sapphire and relatively rare for ruby (S. Karampelas, pers. communication).

Thirty-five thin and ten thin-and-polished sections of corundum-bearing samples and host rocks were studied by optical and a JEOL JSM 5600 scanning electron microscope (SEM) equipped with back-scattered imaging capabilities, respectively, at the Department of Mineralogy and Petrology at the University of Athens (Athens, Greece). Quantitative analyses were carried out at the “Eugen F. Stumpfl” Laboratory installed at the University of Leoben, Austria, using a Superprobe Jeol JXA 8200 wavelength-dispersive electron microprobe (WDS), and at the Department of Mineralogy and Petrology, University of Hamburg (Hamburg, Germany) using a Cameca-SX 100 WDS. Analytical conditions were as follows: at Leoben, 20 kV accelerating voltage, 10 nA beam current, 1 µm beam diameter. Peak and backgrounds counting times were 20 and 10 s for major and 40 and 20 s for trace

elements, respectively. The X-ray lines used were AlK α , SiK α , TiK α , GaK α , FeK α , CeL α , VK α , MgK α , CrK α , and CaL α . The standards used were: corundum for Al, wollastonite for Si and Ca, rutile for Ti, GaAs for Ga, ilmenite for Fe, synthetic V for V, chromite for Mg and Cr. At Hamburg, accelerating voltage of 20 kV, a beam current of 20 nA and counting time of 20 s. The X-ray lines used were: AlK α , SiK α , TiK α , GaK α , FeK α , CeL α , VK α , MgK α , CrK β , and CaL α . The standards used were: andradite and vanadinite (for Si, Ca and V), and synthetic Al₂O₃ (for Al), TiO₂ (for Ti), Fe₂O₃ (for Fe), Cr₂O₃ (for Cr), Ga₂O₃ (for Ga) and MgO (for Mg). Corrections were applied using the PAP online program [32].

Table 1. Sample description of the studied Greek corundum crystals.

| Sample | Variety | Color | Host Rock | Locality |
|--------------------------------------|----------|----------------|------------------|-------------------|
| Dr1a, Dr1b, Dr2 | Ruby | Red | Pargasite-schist | Paranesti, Drama |
| Go1a, Go1b | Sapphire | Blue-colorless | Marble | Gorgona, Xanthi |
| Go5a | Sapphire | Pink-purple | Marble | Gorgona, Xanthi |
| Go5b | Sapphire | Pink | Marble | Gorgona, Xanthi |
| Nx1a, Nx2a, Nx2b, Nx3a, Nx3b, Nx4 | Sapphire | Blue-colorless | Plumasite | Naxos (Kinidaros) |
| Nx1b | Sapphire | Purple | Plumasite | Naxos (Kinidaros) |
| Nx5a | Sapphire | Blue | Metabauxite | Naxos (Kavalaris) |
| Nx5b | Sapphire | Pink | Plumasite | Naxos (Kinidaros) |
| Ik1a, Ik1b | Sapphire | Blue | Metabauxite | Ikaria |

LA-ICP-MS analyses were conducted at the CODES ARC Centre of Excellence in Ore Deposits of the University of Tasmania, Australia, and the Institute of Mineralogy, University of Münster, Germany. Analytical conditions were as follows: The LA-ICP-MS analysis at the CODES was performed under standard procedures using a New Wave UP-213 Nd: YAG Q-switched Laser Ablation System coupled with an Agilent HP 4500 Quadrupole ICP-MS. The international standard NIST 612 was used as the primary standard to calculate concentrations and correct for ablation depth, and the basaltic glass BCR-2 was used as the secondary standard. Analyses were standardized on the theoretical Al content for corundum at Al 529,227 ppm, with an error in analytical precision of 2–3%. Corundum sample ablation at the University of Münster was done with a pulsed 193 nm ArF excimer laser (Analyte G2, Photon Machines). A repetition rate of 10 Hz and an energy of ~4 J/cm² were used throughout the entire session. The beam spot diameter was set to 35 μ m. Trace element analysis has been carried out with an Element 2 mass spectrometer (ThermoFisher). Forward power was 1250 W and reflected power <1 W, gas flow rates were 1.2 L/m for He carrier gas, 0.9 L/m and 1.2 L/m for the Ar-auxiliary and sample gas, respectively. Argon cooling gas flow rate was set to 16 L/min. Before starting analysis, the system was tuned on a NIST 612 reference glass measuring ¹³⁹La, ²³²Th and ²³²Th¹⁶O to get stable signals and high sensitivity, as well as low oxide rates (²³²Th¹⁶O/²³²Th < 0.1%) during ablation. A total of 30 elements were quantitatively analyzed using the NIST 612 glass as an external standard and ²⁷Al as internal standard, which had previously been determined by electron microprobe. Overall time of a single analysis was 60 s (20 s for background, 40 s for peak after switching laser on). Concentrations of measured elements were calculated using the Glitter software [33,34]. Standard reference glass BHVO-2G and BIR1-G were analyzed in order to monitor for precision and accuracy in the silicate phases in the course of this study. The obtained results match the published range of concentrations given in the GeoReM database (version 23).

Fluid inclusions studies were carried in a total of 14 double-polished sections prepared at the Department of Mineralogy, Petrology and Economic Geology of the Aristotle University of Thessaloniki (Thessaloniki, Greece). Routine heating and freezing runs were performed at a LINKAM THM-600/TMS 90 heating–freezing stage coupled to a Leitz SM-LUX-POL microscope. Calibration of the stage was achieved using organic standards with known melting points, and the H₂O phase transition from ice to liquid; the precision of the measurements, including reproducibility, was ± 0.2 °C. The SoWat program [35] was used to process fluid inclusion data.

Oxygen isotope analyses were performed at the Scottish Universities Environmental Research Centre, Glasgow, Scotland. The oxygen isotope composition of corundum was obtained using a modification of the CO₂ laser fluorination system similar to that described by Sharp [36], which was similar applied by Giuliani et al. [14]. The method involves the complete reaction of ~1 mg of ground corundum. This powder is heated by a CO₂ laser, with ClF₃ as the fluorine reagent. The released oxygen is passed through an in-line Hg-diffusion pump before conversion to CO₂ on platinized graphite. The yield is then measured by a capacitance manometer. The gas-handling vacuum line is connected to the inlet system of a dedicated VG PRISM 3 dual-inlet isotope-ratio mass spectrometer. Duplicate analyses of corundum samples suggest that precision and accuracy are $\pm 0.1\text{‰}$ (1σ). All oxygen isotope ratios are shown in $\delta^{18}\text{O}$ (‰) relative to Vienna standard mean ocean water (VSMOW).

3. Geological Setting

3.1. Regional Geology

The Hellenide orogen formed as a result of the collision between the African and Eurasian plates above the north-dipping Hellenic subduction zone from the Late Jurassic to the present [37–39]. From north to south, it consists of three continental blocks (Rhodopes, Pelagonia, and Adria-External Hellenides) and two oceanic domains (Vardar and Pindos Suture Zones). In the Aegean region, continuous subduction of both oceanic and continental lithosphere beneath the Eurasian plate since the Early Cretaceous resulted in a series of magmatic arcs from the north (Rhodope massif) to the south (Active South Aegean Volcanic Arc) [40]. The geodynamic evolution of Hellenides is characterized by a collisional phase taking place during the Mesozoic, followed by a continuous southward slab retreat in a back-arc setting, started at the Eocene but still ongoing, that triggered large-scale extension concomitant with thrusting at the southern part of the Hellenic domain [39,41]. The gem corundum deposits in Greece are spotted in two tectono-metamorphic units of the greater Hellenides Orogen: the Rhodope- and the Attico-Cycladic Massifs [29,30,42].

3.1.1. Rhodope Massif

The Rhodope Massif is considered part of the European continental margin [41,43]. It is a heterogeneous crustal body composed in its eastern and central parts of two sub-domains (Figure 1): the Northern Rhodope Domain and the Southern Rhodope Core Complex (both separated by the Nestos thrust fault and the Nestos Suture Zone) [41]. The Northern Rhodope Domain consists of a Lower unit of high-grade basement including orthogneisses derived from Permo-Carboniferous protoliths; this Unit includes four metamorphic core complexes (the Arda, Biala Reka-Kechros, and Kesebir-Kardamos migmatitic domes) which are considered to be equivalent to orthogneisses in the Southern Rhodope Core Complex (SRCC) [41,44]. The latter also consists of Triassic marbles with intercalated amphibolitic and metapelitic rocks [44,45].

The upper tectonic unit of the Northern Rhodope Domain includes high-grade basement rocks that have both continental and oceanic affinities, and with protoliths ranging in age from Neoproterozoic through Ordovician, and Permo-Carboniferous to Early Cretaceous [45]. The rocks of the Intermediate unit experienced high- to ultra-high-pressure metamorphism with subsequent high-grade amphibolite-facies overprint [46]. The Rhodope Massif has undergone a polycyclic alpine orogeny including UHP-eclogitic metamorphism, followed by HP granulite-facies, amphibolite-facies and finally by greenschist facies metamorphic events starting from Jurassic (~200–150 Ma) and lasting up to the Oligocene [47,48]. In the Rhodope region, syn-orogenic exhumation of the metamorphic pile initiated in the early Eocene (~55 Ma) and core complex extension followed the Cretaceous syn-metamorphic SW-directed thrusting [41,43,49,50]. The metamorphic core complexes were progressively exhumed along several ductile- to brittle shear zones, active from ~42–12 Ma [49,51].

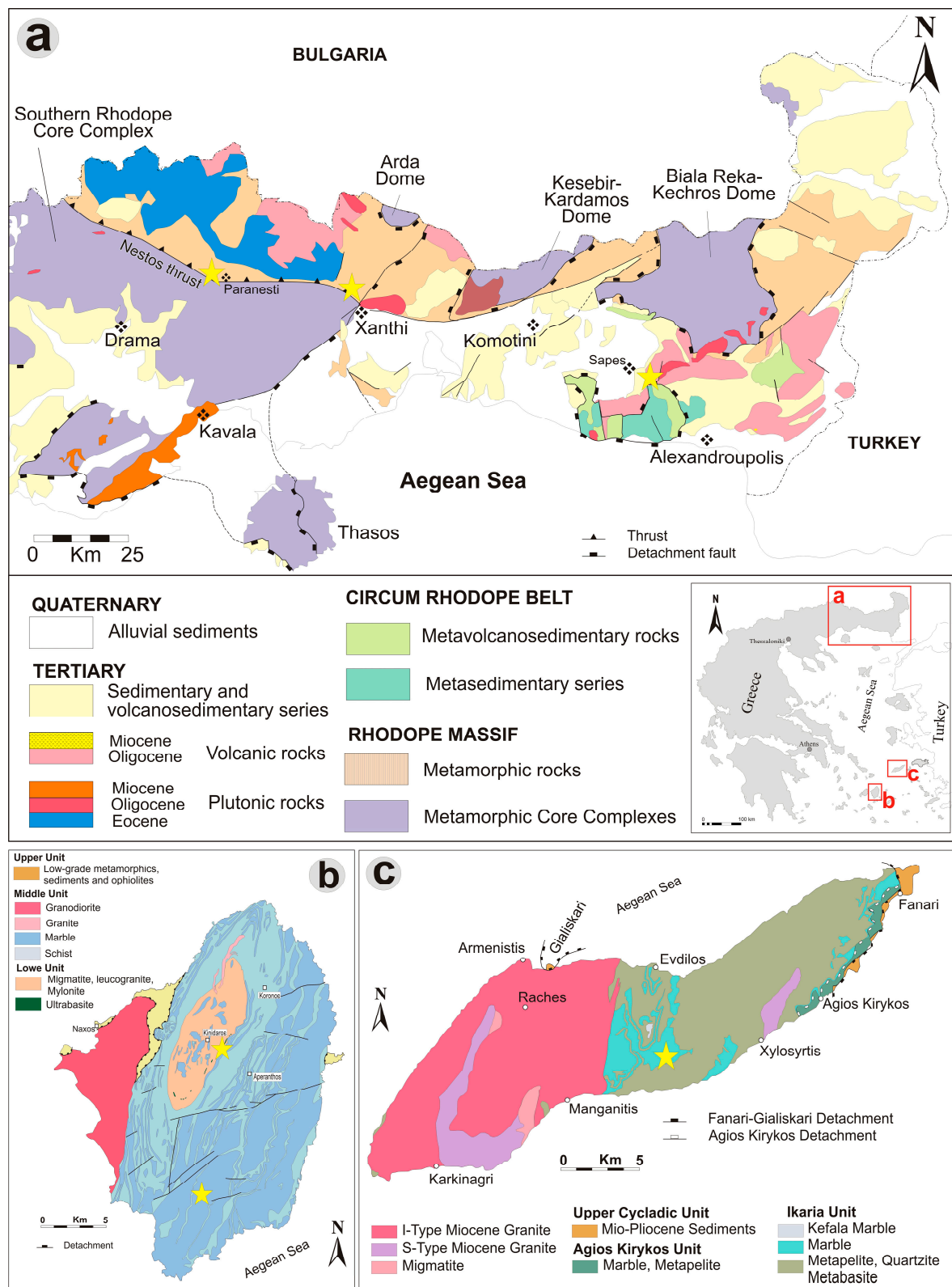


Figure 1. (a) Simplified geological map of eastern Rhodope massif, Greece showing the main tectonic zones and the distribution of Cenozoic igneous rocks (after Melfos and Voudouris [52] and references therein), showing location of corundums at Xanthi, Paranești and Kassiteres/Sapes areas (stars); (b) Geological map of Naxos island showing locations of sapphires in plumasites at Kinidaro and meta-bauxites at Kavalaris Hill (stars) (after Duchêne et al. [53]; modified after Ottens and Voudouris [54]); (c) Geological map of Ikaria showing the location of blue sapphire in Atsida area (after Beaudoin et al. [55]; modified after Ottens and Voudouris [54]). Yellow stars mark the studied corundum occurrences.

Separating the upper and lower tectonic units in the Rhodope complex, the Nestos Suture Zone a NW trending shear zone was extensively studied by Papanikolaou and Panagopoulos [56], Krenn et al. [57], Nagel et al. [58] and Turpaud and Reischmann [45] and is composed from the bottom to the top of the following lithological types: (a) a lower 1-km-thick highly sheared “mélange” zone, consisting of amphibolites, garnet-kyanite schists, migmatites, orthogneisses and marbles; (b) a 1-km-thick sequence of augen-gneisses; (c) two layers of marbles intercalated with amphibolites and mylonitic amphibolites; (d) a layer of ortho-gneisses, characterized by biotite-gneisses with highly migmatized base (Sidironero). Gautier et al. [48] suggest a continuous thrusting tectonism along the Nestos Suture Zone until 33 Ma ago, and Nagel et al. [58] indicate that the Nestos Suture Zone constitutes the base of an Eocene thrusting wedge that also includes UHP units which were probably merged with the Nestos Zone during the thrusting event.

3.1.2. Attico-Cycladic Massif

The Cyclades consist of a lowermost Pre-Alpidic Basement Unit, the intermediate Cycladic Blueschist Unit, and the uppermost Pelagonian Unit [59]. The Blueschist Unit represents a polymetamorphic terrane which tectonically overlies the basement gneiss and consists of a metamorphosed volcano-sedimentary sequence of clastic metasedimentary rocks, marbles, calc-schists, and mafic and felsic meta-igneous rocks [38,39,60]. The Cyclades have been exhumed since the Eocene as metamorphic core complexes formed in low-, medium-, and/or high-temperature environments [50]. An Eocene (~52–53 Ma) high-pressure eclogite- to blueschist-facies metamorphism was followed by syn-orogenic exhumation of the blueschists in a cold retrograde path and then by early Oligocene amphibolite to greenschist facies, and finally, by high-temperature medium-pressure metamorphism and associated migmatites in the early Miocene [37,60–63]. The amphibolite to greenschist metamorphic event occurred during extension-related exhumation and was coeval with back-arc extension at the Rhodopes in northern Greece [64–66]. Exhumation of the Cycladic rocks as metamorphic core complexes was accommodated during the Oligocene–Miocene by several ductile to brittle detachment systems. The extensional event also allowed for various granitoids (granite, granodiorite, leucogranite) to be intruded throughout the Cyclades between 15 and 7 Ma [64].

On Naxos island, a migmatitic dome (pre-alpine basement), is overlain by the Blueschist unit containing alternating layers of marbles, schists and gneisses, and by the upper Pelagonian tectonic unit (Figure 1b). Blueschist relics at the SE part of the island indicate temperatures from 400 to 460 °C at minimum pressures of 7–9 kbar [21] for the high-pressure/low-temperature (HP/LT) Eocene metamorphic event. The metamorphic grade of the Oligocene–Miocene event increases from 400 °C at 6 kbar in marbles, schists, gneisses and amphibolites at the SE of the island, towards the core of the dome, where migmatites in the leucogneissic and amphibolite-facies sillimanitic schists rocks, suggest temperatures up to 700 °C at 6–8 kbar [21,67–70]. Jansen and Schuiling [67] distinguished six metamorphic zones (I–VI) at Naxos island based on mineral isograds. Maximum temperatures are 420 °C for zone I, inferred by the presence of diaspore; 420 to 500 °C (appearance of biotite) for zone II; 500 °C to 540–580 °C (disappearance of chloritoid) for zone III, 540–580 °C to 620–660 °C (kyanite-sillimanite transition) for zone IV, 620–660 °C to 660–690 °C (onset of melting) for zone V; and >690 °C for zone VI. The Naxos migmatitic core is surrounded by a discontinuous block of ultramafic (meta-peridotites) lenses, representing a thrust zone along which the metamorphic complex lies on top of the pre-alpine bedrock [71]. The peridotites underwent high-P metamorphism and then, after cooling amphibolite-facies conditions (T~600 °C), were finally re-heated and metamorphosed together with the country rocks. According to Jansen and Schuiling [67], pegmatites penetrating the ultramafic bodies in the sillimanite stability zone, are desilicated and composed of phlogopite, anorthite, corundum, chlorite, zoisite, tourmaline and beryl. Anorthite crystals are composed almost entirely of anorthite (98% An), while margarite can be found in places. According to Andriessen et al. [72] and Katzir et al. [71], aplites and pegmatites are of Early Miocene age (19–20 Ma), and were formed as a result of the crystallization of an in situ anatectic liquid, that was produced during the high-T

metamorphic event. They represent a system that channeled fluids through the leucogneissic core to the lower metamorphic unit and resulted in the metasomatization of peridotites and in situ recrystallization of the peridotitic blackwalls. Corundum-bearing emery deposits occur in the metamorphic zones I–V following the increase in metamorphic grade from SE towards NW to the migmatite core [21,73].

Ikaria Island (Figure 1c), similarly to Naxos, represents a Miocene migmatite-cored metamorphic core complex, where peak-metamorphic temperatures range from 390 °C in the upper parts of the structure down to 625 °C in the core of the dome in the vicinity of migmatites and S-type granite [55,74]. Three main tectonic units are distinguished and are, from bottom to top, the Ikaria, Agios Kirykos and Fanari units, limited by two major shear zones [55,75,76]. The non-metamorphic Fanari unit consists of Miocene to Pliocene sandstones, conglomerates and ophiolitic molasses. The intermediate Agios Kirykos unit (previously called the Messaria unit) consists of alternating marble and metapelite layers, metamorphosed in greenschist-facies conditions. Finally, the Ikaria unit is composed of amphibolite-facies (ca. 6–8 kbar and 600–650 °C) metasediments including micaschist and marble layers and minor metabasites. Peak-metamorphic conditions were retrieved from the basal parts of the succession. Two synkinematic granitic bodies intrude the Ikaria unit: (a) an I-type Bt-granite (Raches granite) in the western part of the island, with K-Ar ages of 22.7 Ma [64]; and (b) an S-type Bt-Ms-granite (Xilosirtis granite) in the southern part of the island, with Rb-Sr ages of 18.1 Ma [64]. Liati and Skarpelis [77], Iliopoulos and Katagas [24], and Iliopoulos [75] studied the Ikaria metabauxitic rocks hosted in marbles of the Ikaria unit, and recorded a Jurassic age for the formation of bauxitic deposits, and upper greenschist to lower amphibolite-facies conditions for their metamorphism.

3.2. Local Geology

3.2.1. Xanthi

The Gorgona-Stirigma corundum occurrence is stratiform and distributed in marble layers (Figure 2a), reaching up to 50 m width, alternating with eclogitic amphibolites and gneisses [22,27,42]. The chemical composition of the marbles varies widely, highly locally impure marbles, rich in alumino-silicate minerals, are characterized by a mineralogical assemblage composed of calcite, dolomite, corundum, spinel, pyrophyllite, muscovite, paragonite, amphibole, zoisite, margarite, chlorite, olivine, serpentine, phlogopite, rutile, titanite, anorthite, garnet and Ni-tourmaline [22,23,27,42]. Spinel occurs as a rim around corundum crystals. The color of spinel ranges from blue to green and brown. Liati [22] defined the following contact assemblages: calcite-anorthite-zoisite, calcite-corundum-spinel, calcite-corundum-zoisite and margarite-zoisite-anorthite-chlorite. The corundum crystals occur within phyllosilicate-rich micro-shear zones along marble layers. Sapphire is of a pink, orange, purple to blue color, usually of tabular or barrel-shaped euhedral form and reaches sizes of up to 4 cm (Figure 3a–c). In some cases, blue corundum alters to green spinel. Red corundum has also been reported in this area, mainly from zoisite-bearing amphibolites [23], but could not be identified in the present study.

3.2.2. Paranesti

The Paranesti corundum occurrence is stratiform, oriented parallel to the main regional foliation, and distributed mainly in boudin-like lenses of amphibole schist (Figure 2b) [27,30,42]. The outcrops on the surface are spotted west of Perivlepto village at one hillside and one roadside location [30]. In the first site, the corundum-bearing amphibole schist lenses are surrounded by a narrow clinocllore schist zone and occur together with boudins of corundum-kyanite-amphibole schists. The schists are intruded by white-colored quartz-feldspar-mica-garnet pegmatitic veins, which do not present characteristics of desilication (Figure 2c). In the second site, the lenses are hosted by amphibolites, intercalated with kyanite-bearing gneisses and kyanite-amphibole-chlorite schists. Again, the transition from amphibolitic lithology towards corundum mineralization is made through a clinocllore-rich schist zone. Ruby crystals from Paranesti, range in size from <1 mm to 50 mm size (average size 5–10 mm, and are of pale pink to deep red color [30]. Their morphology is mainly flat tabular with

basal planes paralleling the orientation of the main regional foliation [30], and less commonly prismatic and barrel-shaped (Figure 3d,e). They occur together with pargasite, which is the main amphibole of the assemblage, forming a similar image with Tanzanian rubies which are surrounded by zoisite. The ruby crystals coexist locally with kyanite (Figure 3f).

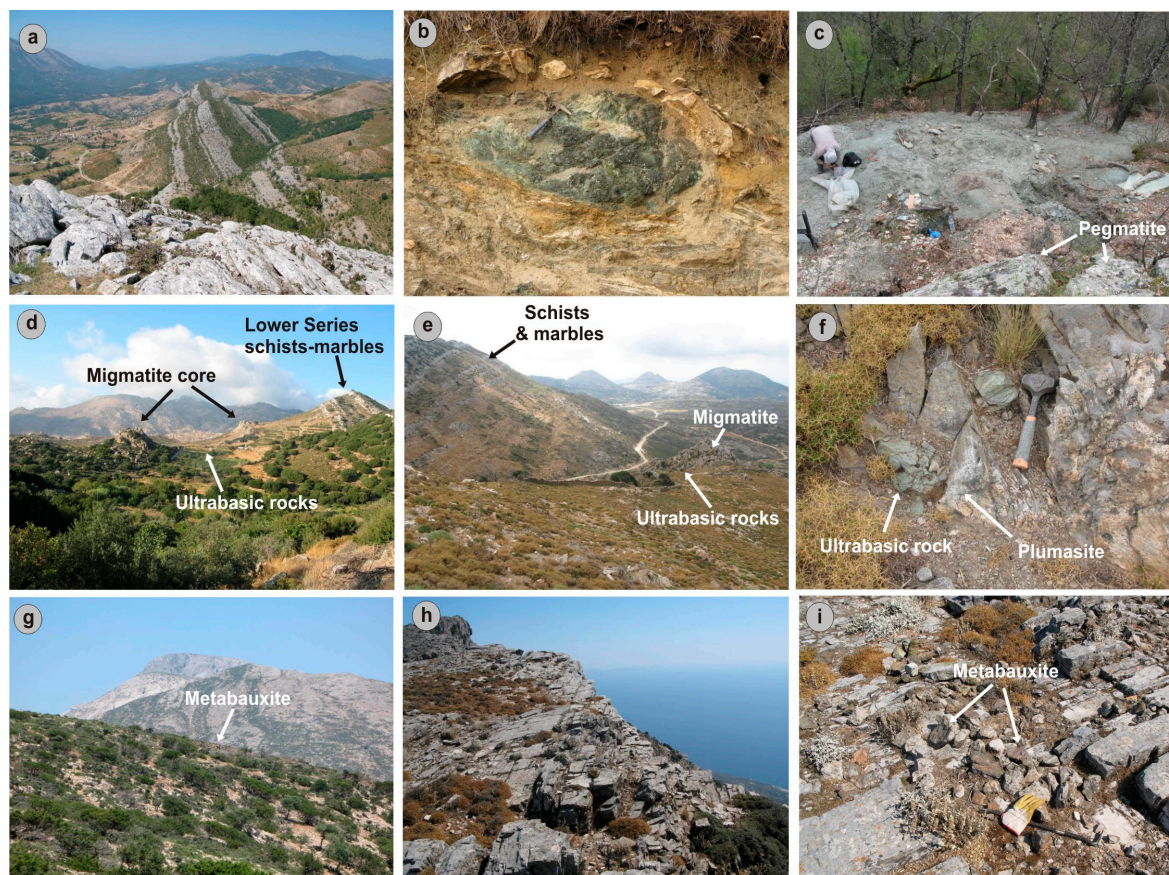


Figure 2. Field photographs demonstrating the geological setting of the ruby and sapphire occurrences in Greece. (a) Marble layers alternating with eclogitic amphibolites at Gorgona/Xanthi; (b) Boudinaged hornblende schists, intercalated within eclogitic amphibolites, marbles and metapegmatites at Paranesti/Drama; (c) The main ruby working at Paranesti. The pegmatite body at the lower part of the photograph shows no desilification; (d,e) Ultrabasic rocks between the migmatite dome-like core and the overlying kyanite-sillimanite grade schists and marbles in the two plumasite localities east of Kinidaros, Naxos island; (f) Corundum-bearing plumasite at the contact to ultrabasites at the locality shown in Figure 2e; (g) Panoramic view of the metabauxite-bearing marbles at Kavalaris Hill, southern Naxos island; (h) Panoramic view for the metabauxite-bearing marbles of Ikaria unit; (i) Corundum-bearing metabauxite lenses within the Ikaria unit marbles.

3.2.3. Naxos

The corundums studied from Naxos island occur in two localities, representing different geological environments.

(a) In the central part of the island and about 2 km east and southeast of Kinidaros, two corundum-bearing plumasites (desilicated pegmatites) were studied (Figure 2d–f) [27,29,42]. The meta-peridotites occurred initially as lenses of few to several tens of meters size and are surrounded by phlogopitite, which formed at the contact between the metaperidotites and the intruding pegmatites. Today, most of the plumasites and metaperidotites in these two localities occur as loose fragments mainly due to erosion and agricultural activities in the area.



Figure 3. Field photographs and handspecimens demonstrating gem corundum crystals of Greece: (a–c) Pink, blue, to purple sapphires within Xanthi marbles; (d,e) Deep red-colored ruby with both tabular and barrel-shaped crystals within pargasite schist from Paranești/Drama; (f) Ruby associated (replacing) kyanite, Paranești/Drama; (g) Barrel-shaped blue and colorless sapphires hosted within anorthite-rich desilicated pegmatite (plumasite) and associated with phlogopite and tourmaline (schorlite) from the first Kinidaros locality, Naxos island; (h) Purple to pink sapphire within plumasite the later rimmed by phlogopite at the left part, second Kinidaros locality, Naxos island; (i) Blue sapphire in fissures within metabauxite at Kavalaris Hill, southern Naxos island; (j,k) Blue sapphires and margarite as free growing crystals of probably hydrothermal origin within fissure of metabauxites, Ikaria island.

The plumasites are surrounded by an up to 20-cm-wide zone of phlogopite and chlorite (blackwall) (Figure 3g). Within the plumasites, colorless to blue, purple and pink corundum may occur either as isolated crystals within the plagioclase matrix, and/or associated with tourmaline, and phlogopite (Figure 3g,h). Purple to pink sapphires have been also found entirely enclosed in phlogopite in the blackwalls. The sapphire crystals are barrel-shaped, display macroscopic color zoning from colorless cores to blue rims or pink cores to purple rims and reach sizes up to 3 cm [27,42].

(b) In the southern part of the island, close to Kavalaris Hill (Figure 2g), corundum represents a single mineral rock termed “corundite” by Feenstra and Wunder [73], which was formed by the dissociation of former diasporites, in meta-carstic bauxites during prograde regional metamorphism. This first corundum occurrence in metabauxites also recorded as corundum-in isograd ($T \sim 420\text{--}450\text{ }^{\circ}\text{C}$ and $P \sim 6\text{--}7\text{ kbar}$, [73]), separates diasporites with the assemblage diasporite-chloritoid-muscovite-paragonite-calcite-hematite-rutile from emery characterized by corundum-chloritoid-muscovite-paragonite-margarite-hematite-rutile. Corundum and chloritoid intergrowths occur as a rim in metabauxites, while the corundum crystals occur mainly in the contact between marbles and metabauxites. The corundum from this locality does not occur in well-shaped crystals; it is, rather, massive, and of blue color (Figure 3i).

3.2.4. Ikaria

The metabauxite occurrence is located on mountain Atheras (Figure 2h) [20,75]. Already Iliopoulos [75], reported the presence of corundum as mineralogical constituent of meta-bauxite (emery) lenses occurring within dolomitic and calcic marble, which lies on top of gneiss, both being part of the Ikaria unit. In this area, four main layers of metabauxites, of up to 1 m width, were detected (Figure 2i). However, the corundum megacrysts described by Voudouris et al. [27,42] represent a second, late, generation of corundum formation within the emeries, since they fill together with margarite extensional fissures and networks of veins discordant to the metabauxite foliation (Figure 3j,k) [27,42]. The corundums are deep-blue in color, tabular to euhedral, reaching sizes up to 4 cm and are accompanied by Fe-chlorite, hematite, rutile and diasporite.

4. Mineralogy

The Paraneesti rubies are dull to transparent, exhibiting clear parting and polysynthetic twinning. The rubies are associated with edenitic hornblende and tremolite, and rimmed by margarite, muscovite, chlorite and chromian spinel (Figure 4a,b and Figure 5a,b). The ruby crystals are surrounded by a margarite rim. Spinel appears as the main component of primary inclusions in the rubies. The association of ruby in this deposit is pargasite, chlorite (mainly clinocllore and rarely nimite), margarite, tremolite and/or monazite, while for the host rocks the assemblage is pargasite, anorthite, clinozoisite, chlorite and monazite. The Paraneesti rubies are rimmed by Cr-bearing spinel and also include ulvospinel. Corundum is in equilibrium with amphibole, while in a later, retrograde stage margarite-muscovite, Cr-bearing spinel, orthoclase, chlorite, smectite and vermiculite, rim and/or replace corundum. Cr-bearing spinel is replaced by chlorite.

The corundums from Xanthi are transparent, with very clear parting and fine cracks. Polysynthetic twinning is common. Corundum may be isolated within the carbonate matrix (Figure 4c) or rimmed by amesite (an Al-rich serpentine member), margarite, titanite or by brown and green spinel. Blue sapphires are zoned, with alternating deep blue and colorless domains (Figure 4c). This zoning, or irregular color distribution in the sapphires, is attributed to different Fe and Ti contents in the crystals (see next paragraph). Ni-bearing brown tourmaline accompanying corundum in the paragenesis contains up to 4.4 wt. % NiO, much higher than the Ni content reported in tourmaline from Samos by Henry and Dutrow [78].

The sapphire crystals from Naxos present strong pleochroism with their color ranging from dark blue to colorless (Figure 4d–f). They are transparent, with smaller or bigger inner fractures. Hexagonal barrel-shaped corundum crystals exhibit blue color zoning. The blue color of corundum is

observed either as a blue core surrounded by a white rim or as a blue-zoned outer rim surrounding a colorless core. Polysynthetic twinning is observed along the colorless parts of the crystals. Sapphires are associated with anorthite, phlogopite, zircon, margarite, muscovite, tourmaline and chlorite (Figures 4d–f and 5c–i). The sapphires are enveloped by an assemblage consisting of oligoclase/labradorite-orthoclase-muscovite and then by phlogopite, chlorite (Figure 5c–h). In sample Nx1, blue sapphire associated with phlogopite is rimmed by an intergrowth of oligoclase, anorthite, orthoclase and muscovite. Margarite, zircon, diaspore, phlogopite and chlorite are included in blue sapphire; however, it is considered that margarite, diaspore and chlorite are retrograde minerals postdating corundum formation (this study). In samples Nx4 and Nx4a, blue sapphire includes phlogopite, zircon and apatite and surrounded by anorthite, muscovite and tourmaline with minor amounts of monazite and chlorite. Phlogopite and anorthite are replaced by muscovite, margarite and chlorite. Tourmaline postdates anorthite and muscovite.

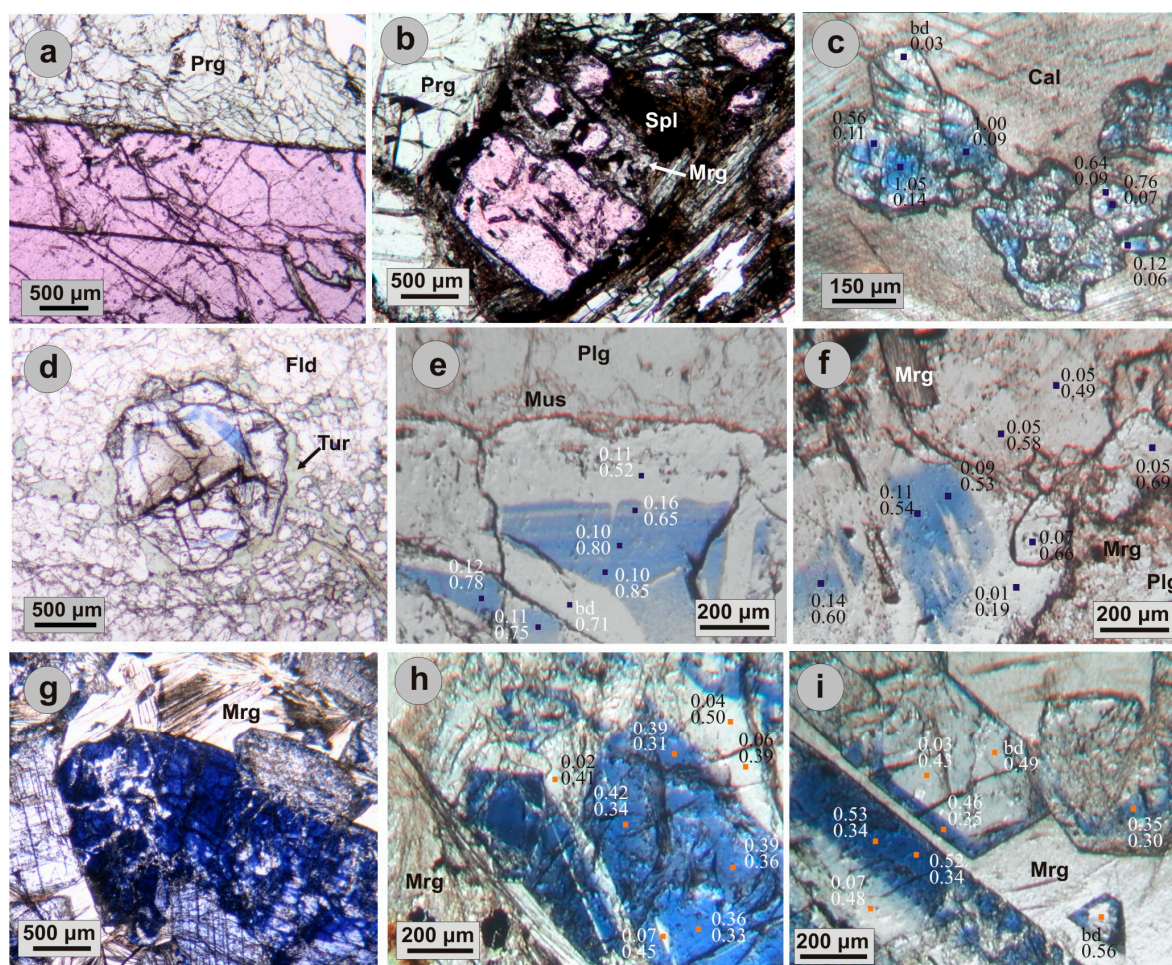


Figure 4. Microphotographs (plane polarized light) demonstrating mineralogical assemblages, color- and chemical zoning of corundum-bearing assemblages from Greece. Values in microphotographs (c,e,f,h,i) correspond to TiO₂ and Fe₂O₃ content in wt. % (upper and lower values, respectively) as obtained by electron probe microanalyses. (a,b) Ruby associated with pargasite (Prg) from Paranesti, Drama area. Note replacement of ruby by spinel (Spl) and margarite (Mrg) in Figure 4b (sample Dr1a); (c) blue to colorless sapphires included in calcite, Xanthi area (sample Go1b); (d,e) Zoned blue to colorless sapphires within anorthite (Plg) and rimmed by tourmaline (Tur) and muscovite (Mus), Kinidaros, Naxos island (sample Nx4); (f) Sapphire with blue core and colorless rim associated with margarite (Mrg) and anorthite (Plg), Kinidaros, Naxos island (sample Nx3); (g) Idiomorphic deep blue colored sapphire crystals surrounded by margarite, Ikaria island (sample Ik1b); (h,i) Zoned blue to colorless idiomorphic sapphires, surrounded by margarite, Ikaria island (sample Ik2).

On Ikaria Island, blue sapphires in the metabauxites are accompanied by the assemblage margarite + chloritoid + hematite/ilmenite + rutile (Figures 4g–i and 5j–l). Chloritoid fill fractures and also occurs as inclusions in margarite. The retrogression has continued to low temperatures as suggested by the presence of diaspore replacing corundum (Figure 4j–l) and chlorite replacing chloritoid. Corundum forms colorless cores and deep blue rims (Figure 4h,i). While transparent, their blue color is quite dark, with colorless spots appearing all over their surface. Corundum includes ilmenite, hematite, ulvospinel, rutile and zircon. In addition, a Zn-bearing green colored spinel, which forms solid solution between hercynite and gahnite, has been reported with chlorite and/or margarite by Iliopoulos [75] and Iliopoulos and Katagas [24].

In sample Ik1a, Ik1b, and Ik2 blue sapphire is surrounded by margarite, chlorite and green-spinel. Chlorite fills fractures and represents latest deposition. Chloritoid, ilmenite, ulvospinel, rutile, Ti-hematite and zircon occur as inclusions in sapphire. Sapphire is associated with hematite, zircon and chloritoid and is replaced by diaspore and margarite.

5. Mineral Chemistry

5.1. EPMA

Electron probe microanalyses (EPMA) for the Greece corundums are presented in Table 2. EPMA data from Paranesti/Drama rubies showed an extreme enrichment in Cr_2O_3 , which reaches up to 2.65 wt. %, with the higher concentrations being consistent with intense red-colored grains. Beyond Cr_2O_3 , the Paranesti rubies are characterized by moderate Fe_2O_3 values (up to 0.44 wt. %) and by traces of MgO , Ga_2O_3 , SiO_2 , TiO_2 and CaO , which range from below detection up to 0.17, 0.15, 0.09, 0.05 and 0.02 wt. %, respectively. Finally, V_2O_3 content is mostly below detection, but in some cases values up to 0.07 wt. % were detected.

Colored sapphires from Gorgona/Xanthi are characterized by elevated contents of TiO_2 , MgO and Fe_2O_3 . The blue color varieties show the highest TiO_2 content, which reaches up to 1.05 wt. %, while MgO and Fe_2O_3 reach up to 0.27 and 0.22 wt. %, respectively. In the pink-colored grains, TiO_2 and Fe_2O_3 contents are significantly lower (up to 0.17 and 0.06 wt. %, respectively) in comparison to the blue ones, but MgO content increases up to 0.36 wt. %. SiO_2 and CaO values are generally below 0.08 wt. %, but in one analysis SiO_2 is 0.51 wt. %, probably indicating a fine-grained silicate inclusion. V_2O_3 content tends to be higher in the pink varieties rather than the colorless to blue, with values ranging from below detection to 0.06 and 0.01 wt. %, respectively. Pink-colored grains contain more than double Ga_2O_3 content (up to 0.17 wt. %) compared to the blue ones (up to 0.07 wt. %). Finally, colorless grains display very low TiO_2 content (from below detection up to 0.12 wt. %) and similar Fe_2O_3 contents to the blue domains.

In colored sapphires from the Naxos plumasite, Fe_2O_3 is the dominant impurity. In the blue varieties, the Fe_2O_3 content reaches up to 0.93 wt. %, and decreases significantly in the colorless (up to 0.69 wt. %), pink- (up to 0.50 wt. %) and the purple-colored grains (up to 0.34 wt. %). A similar decreasing trend is remarked for the Ga_2O_3 content, which reaches up to 0.18 wt. % in the white to blue sapphires, and decreases slightly in the pink and purple varieties, reaching up to 0.15 and 0.10 wt. %, respectively. On the other hand, TiO_2 and MgO seem both to follow a different trend: the highest values for both oxides characterize the purple-colored grains (up to 0.58 and 0.54 wt. %, respectively). Blue grains display intermediate values (up to 0.38 and 0.49 wt. %), followed by the pink grains (up to 0.27 and 0.35 wt. %), respectively. TiO_2 content in the colorless areas ranges from below detection to 0.12 wt. % similarly to the blue domains. The Cr_2O_3 content is up to 0.1 wt. % in the colorless to blue and purple varieties, and almost doubles in the case of pink sapphires (up to 0.18 wt. %). Traces of SiO_2 , V_2O_3 and CaO were also detected in all samples (up to 0.13, 0.09 and 0.03 wt. %, respectively).

Blue sapphires from Ikaria island appear enriched in TiO_2 and Fe_2O_3 values, which reach up to 0.69 and 0.57 wt. %, respectively. SiO_2 shows a wide range from below detection to 0.44 wt. %, while MgO content is constantly low (up to 0.05 wt. %). The Cr_2O_3 and Ga_2O_3 content are almost fixed,

reaching up to 0.14 wt. %. Traces of V_2O_3 and CaO were also detected (up to 0.04 and 0.02 wt. %, respectively). Colorless domains are characterized by very low TiO_2 values, which range from below detection up to 0.12 wt. %.

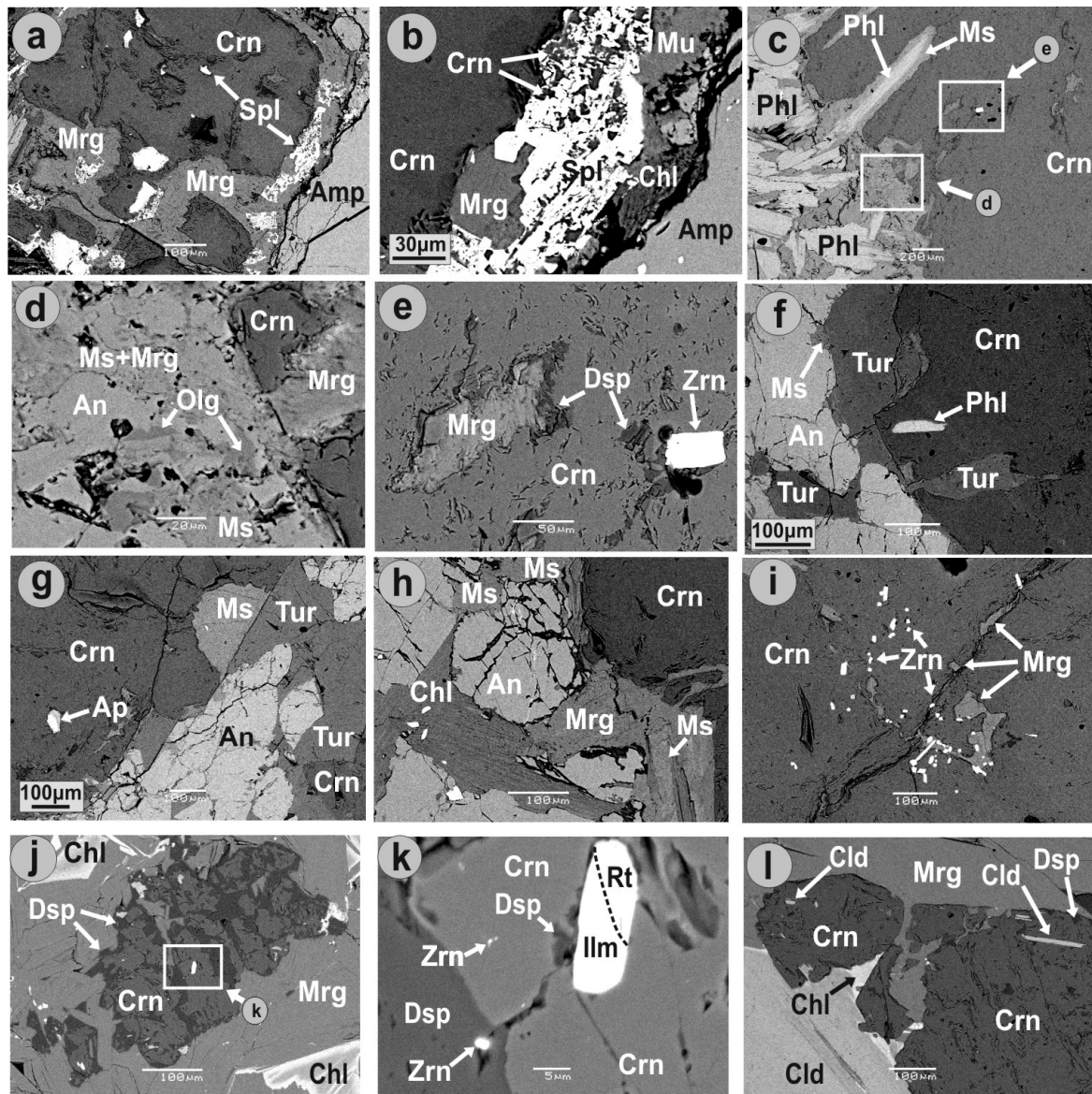


Figure 5. Microphotographs (SEM-BSE images) demonstrating mineralogical assemblages of corundum-bearing assemblages from Greece. (a,b) Ruby (Crn) including and rimmed by chromian spinel (Spl), margarite (Mrg), muscovite (Mu), chlorite (Chl) and pargasitic hornblende (Amp) (sample Dr1, Paranesti/Drama); (c,d) Blue sapphire (Crn) in association with anorthite (An) and phlogopite (Phl) replaced by muscovite (Mus), margarite (Mrg), and oligoclase (Olg) (Naxos island, sample Nx1); (e) Zircon (Zrn) is included in sapphire, diaspore (Dsp) and margarite (Mrg) fill fractures and are retrograde minerals. Naxos island, sample Nx1); (f,g) Blue sapphire including phlogopite and fluorite (Fl) is associated with anorthite (An) and replaced by tourmaline (Tur) and muscovite (Mus) (Naxos island, sample Nx4); (h) Blue sapphire and anorthite are rimmed by muscovite, margarite and chlorite (Chl) the late probably replacing phlogopite (Naxos island, sample Nx4a); (i) Blue sapphire including zircon is replaced by margarite (Naxos island, sample Nx4a); (j–l) Blue sapphire associated with margarite includes and replaces chloritoid (Cld) and are retrogressed to diaspore and chlorite, respectively. Zircon and Ilmenite (Ilm), rutile (Rt) are included in corundum (Ikaria island, sample Ik2).

Table 2. Chromophores and key trace elements electron probe microanalyses (EPMA) (wt. %) of the Greek corundum crystals.

| Sample | Color | ppm | MgO | Al ₂ O ₃ | SiO ₂ | CaO | TiO ₂ | V ₂ O ₃ | Cr ₂ O ₃ | Fe ₂ O ₃ | Ga ₂ O ₃ | Total |
|-----------------------|----------------|------|------|--------------------------------|------------------|-------|------------------|-------------------------------|--------------------------------|--------------------------------|--------------------------------|--------|
| Dr1a (<i>n</i> = 8) | red | aver | bd | 96.96 | 0.03 | 0.01 | 0.01 | 0.01 | 1.82 | 0.39 | 0.02 | 99.23 |
| | | min | bd | 96.52 | 0.03 | bd | bd | bd | 1.74 | 0.34 | bd | 98.80 |
| | | max | bd | 97.39 | 0.04 | 0.02 | 0.01 | 0.01 | 1.99 | 0.43 | 0.09 | 99.66 |
| Dr1b (<i>n</i> = 13) | red | aver | bd | 96.98 | 0.04 | 0.01 | 0.01 | 0.01 | 2.14 | 0.37 | 0.02 | 99.55 |
| | | min | bd | 96.13 | 0.02 | bd | bd | bd | 1.48 | 0.33 | bd | 98.95 |
| | | max | bd | 97.58 | 0.09 | 0.01 | 0.01 | 0.01 | 2.65 | 0.44 | 0.07 | 100.10 |
| Dr2 (<i>n</i> = 8) | red | aver | 0.02 | 99.79 | 0.01 | 0.01 | 0.01 | 0.01 | 0.32 | 0.19 | 0.05 | 100.41 |
| | | min | bd | 99.18 | bd | bd | bd | bd | 0.18 | 0.15 | bd | 99.78 |
| | | max | 0.17 | 100.65 | 0.03 | 0.02 | 0.05 | 0.074 | 0.43 | 0.21 | 0.15 | 101.30 |
| Go1a (<i>n</i> = 11) | blue-colorless | aver | 0.07 | 98.02 | 0.09 | 0.01 | 0.59 | 0.01 | 0.04 | 0.11 | 0.01 | 98.94 |
| | | min | 0.02 | 97.37 | bd | bd | bd | bd | bd | 0.07 | bd | 98.19 |
| | | max | 0.27 | 98.61 | 0.51 | 0.01 | 0.94 | 0.01 | 0.08 | 0.14 | 0.04 | 99.36 |
| Go1b (<i>n</i> = 15) | blue-colorless | aver | 0.04 | 99.21 | 0.03 | 0.02 | 0.56 | 0.01 | 0.01 | 0.11 | 0.02 | 100.00 |
| | | min | bd | 98.46 | 0.01 | bd | bd | bd | bd | 0.031 | bd | 99.70 |
| | | max | 0.10 | 99.73 | 0.07 | 0.08 | 1.05 | 0.01 | 0.05 | 0.21 | 0.07 | 100.38 |
| Go5b (<i>n</i> = 14) | pink | aver | 0.05 | 100.93 | 0.01 | 0.01 | 0.06 | 0.01 | 0.03 | 0.04 | 0.05 | 101.18 |
| | | min | bd | 100.22 | bd | bd | bd | bd | bd | bd | bd | 100.40 |
| | | max | 0.36 | 101.58 | 0.03 | 0.02 | 0.17 | 0.06 | 0.06 | 0.06 | 0.17 | 101.99 |
| Ik1a (<i>n</i> = 8) | blue | aver | bd | 97.88 | 0.35 | 0.01 | 0.23 | 0.01 | 0.05 | 0.36 | 0.03 | 98.90 |
| | | min | bd | 97.08 | 0.24 | bd | bd | bd | bd | 0.27 | bd | 98.16 |
| | | max | bd | 98.45 | 0.44 | 0.016 | 0.53 | 0.04 | 0.13 | 0.50 | 0.12 | 99.36 |
| Ik1b (<i>n</i> = 16) | blue | aver | 0.01 | 99.13 | 0.04 | 0.01 | 0.25 | 0.01 | 0.03 | 0.43 | 0.03 | 99.91 |
| | | min | bd | 98.44 | 0.02 | bd | bd | bd | bd | 0.14 | bd | 99.61 |
| | | max | 0.01 | 99.68 | 0.06 | 0.01 | 0.68 | 0.04 | 0.10 | 0.57 | 0.14 | 100.21 |
| Nx1a (<i>n</i> = 8) | blue-colorless | aver | 0.01 | 98.25 | 0.09 | 0.01 | 0.22 | bd | 0.04 | 0.31 | 0.02 | 98.94 |
| | | min | bd | 97.85 | 0.07 | bd | bd | bd | bd | 0.23 | bd | 98.77 |
| | | max | 0.05 | 98.80 | 0.12 | 0.02 | 0.38 | bd | 0.12 | 0.45 | 0.08 | 99.42 |
| Nx1b (<i>n</i> = 14) | purple | aver | 0.12 | 99.80 | 0.02 | 0.01 | 0.27 | 0.01 | 0.01 | 0.27 | 0.04 | 100.54 |
| | | min | bd | 98.08 | bd | bd | 0.08 | bd | bd | 0.20 | bd | 98.79 |
| | | max | 0.54 | 100.57 | 0.07 | 0.02 | 0.58 | 0.06 | 0.04 | 0.34 | 0.11 | 101.28 |
| Nx2b (<i>n</i> = 22) | blue-colorless | aver | 0.10 | 100.26 | 0.02 | 0.01 | 0.07 | 0.01 | 0.01 | 0.45 | 0.05 | 100.98 |
| | | min | bd | 93.73 | bd | bd | bd | bd | bd | 0.136 | bd | 99.21 |
| | | max | 0.49 | 101.81 | 0.07 | 0.03 | 0.19 | 0.08 | 0.04 | 0.69 | 0.18 | 101.96 |
| Nx3b (<i>n</i> = 15) | blue-colorless | aver | 0.01 | 98.98 | 0.05 | 0.01 | 0.08 | 0.01 | 0.01 | 0.66 | 0.01 | 99.80 |
| | | min | bd | 98.33 | 0.01 | bd | 0.01 | bd | bd | 0.19 | bd | 99.30 |
| | | max | 0.02 | 99.47 | 0.13 | 0.01 | 0.16 | 0.01 | 0.04 | 0.93 | 0.05 | 100.23 |
| Nx4 (<i>n</i> = 16) | blue-colorless | aver | 0.01 | 98.09 | 0.09 | 0.01 | 0.10 | 0.01 | 0.01 | 0.72 | 0.01 | 99.02 |
| | | min | bd | 97.69 | 0.05 | bd | bd | bd | d | 0.52 | bd | 98.67 |
| | | max | 0.01 | 98.55 | 0.12 | 0.01 | 0.17 | 0.01 | 0.01 | 0.85 | 0.05 | 99.43 |
| Nx5b (<i>n</i> = 12) | pink | aver | 0.10 | 100.64 | 0.01 | 0.01 | 0.06 | 0.01 | 0.05 | 0.35 | 0.04 | 101.27 |
| | | min | bd | 97.20 | bd | bd | bd | bd | bd | 0.16 | db | 98.91 |
| | | max | 0.35 | 100.7 | 0.06 | 0.02 | 0.27 | 0.09 | 0.18 | 0.45 | 0.15 | 102.70 |

bd = below detection; aver = average; min = minimum; max = maximum.

5.2. LA-ICP-MS

The trace element results for averages, ranges and critical ratios are listed in Tables 3 and 4. Analyzed rubies from Paranesti/Drama are particularly enriched in Cr (up to 15,347 ppm), and less so in Fe (up to 4348 ppm), with the highest values for both elements coming from the most dark-colored grains. The Mg, Ga and V values are consistently low, (up to 31, 24 and 6 ppm, respectively). The low V contents result in consistent very low V/Cr ratios, typically <1. Calcium and Ti values display wide variations between 117–1444 ppm and 8–148 ppm, respectively, with higher values characterizing the most light-colored grains. Other trace elements are close or below detection limits.

Table 3. Chromophores and key trace elements (Mg and Fe) LA-ICP-MS analyses (ppm) of the Greek corundum crystals and their different chemical ratios.

| Sample. | Color | ppm | Mg | Ti | V | Cr | Fe | Ga | V/Cr | V + Cr/Ga | Fe/Mg | Ga/Mg | Fe/Ti | Cr/Ga |
|-----------------------|----------------|------|-----|------|------|--------|------|-----|--------|-----------|-------|-------|-------|-------|
| Dr1a (<i>n</i> = 8) | red | aver | 15 | 17 | 2.4 | 9814 | 2020 | 14 | 0.0003 | 718 | 162 | 1.11 | 133 | 718 |
| | | min | 8 | 8 | 2 | 8326 | 1799 | 12 | 0.0002 | 602 | 86 | 0.53 | 75 | 602 |
| | | max | 25 | 27 | 2.7 | 12,116 | 2181 | 16 | 0.0003 | 879 | 247 | 1.68 | 225 | 879 |
| Dr1b (<i>n</i> = 13) | red | aver | 17 | 39 | 3.79 | 14,322 | 3795 | 14 | 0.0003 | 998 | 295 | 1.13 | 109 | 998 |
| | | min | 9 | 22 | 3.01 | 11,625 | 3352 | 12 | 0.0002 | 750 | 122 | 0.46 | 68 | 750 |
| | | max | 31 | 58 | 5.71 | 15,347 | 4348 | 16 | 0.0004 | 1252 | 440 | 1.72 | 187 | 1252 |
| Dr2 (<i>n</i> = 8) | red | aver | 17 | 67 | 2.4 | 3289 | 2149 | 20 | 0.0008 | 162 | 157 | 1.48 | 58 | 161 |
| | | min | 13 | 27 | 2.1 | 2431 | 1918 | 19 | 0.0006 | 122 | 91 | 0.95 | 16 | 122 |
| | | max | 24 | 148 | 2.9 | 4056 | 2438 | 24 | 0.0011 | 190 | 209 | 2 | 83 | 189 |
| Go1a (<i>n</i> = 11) | blue-colorless | aver | 380 | 5007 | 90 | 97 | 1096 | 89 | 1.89 | 2.98 | 3.16 | 0.26 | 0.26 | 1.91 |
| | | min | 227 | 1915 | 40 | 35 | 554 | 29 | 0.23 | 1.15 | 1.32 | .07 | 0.10 | 0.29 |
| | | max | 601 | 6462 | 159 | 251 | 1339 | 119 | 4.15 | 7.73 | 5.73 | 0.49 | 0.68 | 6.30 |
| Go1b (<i>n</i> = 15) | blue-colorless | aver | 264 | 3503 | 66 | 70 | 910 | 89 | 1.19 | 1.59 | 4.33 | 0.46 | 0.35 | 0.86 |
| | | min | 78 | 1007 | 23 | 35 | 363 | 64 | 0.26 | 0.84 | 1.66 | 0.14 | 0.12 | 0.30 |
| | | max | 536 | 6361 | 207 | 187 | 1309 | 121 | 2.96 | 3.71 | 9.25 | 0.94 | 1.20 | 2.92 |
| Go5a (<i>n</i> = 8) | pink-purple | aver | 28 | 102 | 20 | 104 | 1291 | 47 | 0.37 | 2.88 | 60 | 2.46 | 24 | 2.46 |
| | | min | 13 | 30 | 5 | 4 | 962 | 9 | 0.04 | 0.34 | 21 | 0.43 | 4.98 | 0.43 |
| | | max | 49 | 205 | 60 | 298 | 1782 | 100 | 1.36 | 8.13 | 130 | 7.45 | 56 | 7.45 |
| Go5b (<i>n</i> = 14) | pink | aver | 35 | 509 | 65 | 297 | 424 | 78 | 0.30 | 4.67 | 14 | 2.54 | 1.45 | 3.83 |
| | | min | 17 | 39 | 47 | 105 | 294 | 72 | 0.04 | 2.13 | 8.17 | 4.42 | 0.51 | 1.27 |
| | | max | 53 | 810 | 79 | 1082 | 494 | 87 | 0.68 | 14.68 | 24 | 6.57 | 9.19 | 14.08 |
| Ik1a (<i>n</i> = 8) | blue | aver | 13 | 1135 | 120 | 222 | 3237 | 85 | 0.57 | 4.04 | 445 | 12 | 3.10 | 2.65 |
| | | min | 5 | 653 | 70 | 168 | 2710 | 72 | 0.22 | 3.30 | 62 | 1.50 | 1.93 | 1.97 |
| | | max | 54 | 1942 | 154 | 313 | 3627 | 93 | 0.84 | 5.29 | 711 | 19 | 4.73 | 4.32 |
| Ik1b (<i>n</i> = 16) | blue | aver | 16 | 1390 | 111 | 224 | 5415 | 94 | 0.49 | 3.54 | 348 | 6.07 | 8.49 | 2.38 |
| | | min | 13 | 267 | 31 | 103 | 3903 | 68 | 0.20 | 2.13 | 207 | 3.54 | 0.93 | 1.52 |
| | | max | 24 | 4508 | 164 | 279 | 7324 | 114 | 0.67 | 5.24 | 491 | 9.76 | 20.3 | 3.21 |
| Nx1a (<i>n</i> = 8) | blue-colorless | aver | 47 | 368 | 16 | 691 | 1532 | 46 | 0.02 | 15 | 35 | 1.06 | 7.32 | 15 |
| | | min | 32 | 105 | 14 | 504 | 1377 | 42 | 0.02 | 11 | 24 | 0.70 | 1.78 | 10 |
| | | max | 71 | 943 | 19 | 851 | 1804 | 53 | 0.04 | 19 | 43 | 1.37 | 14 | 18 |

Table 3. Cont.

| Sample. | Color | ppm | Mg | Ti | V | Cr | Fe | Ga | V/Cr | V + Cr/Ga | Fe/Mg | Ga/Mg | Fe/Ti | Cr/Ga |
|-----------------------|----------------|------|-----|------|----|-----|------|-----|------|-----------|-------|-------|-------|-------|
| Nx1b (<i>n</i> = 14) | purple | aver | 64 | 520 | 22 | 43 | 4677 | 63 | 0.52 | 1.03 | 82 | 1.12 | 12 | 0.48 |
| | | min | 39 | 124 | 15 | 36 | 3324 | 55 | 0.34 | 0.82 | 27 | 0.37 | 4.16 | 0.67 |
| | | max | 199 | 848 | 31 | 48 | 6670 | 76 | 0.86 | 1.14 | 123 | 1.57 | 44 | 0.83 |
| Nx2a (<i>n</i> = 8) | blue-colorless | aver | 45 | 489 | 24 | 3.6 | 3210 | 49 | 14 | 0.55 | 84 | 1.30 | 16 | 0.07 |
| | | min | 24 | 40 | 19 | 0.9 | 2852 | 47 | 1.83 | 0.44 | 42 | 0.67 | 4.15 | 0.02 |
| | | max | 82 | 761 | 36 | 11 | 3474 | 53 | 42 | 0.68 | 127 | 1.99 | 86 | 0.22 |
| Nx2b (<i>n</i> = 22) | blue-colorless | aver | 63 | 560 | 26 | 51 | 4241 | 60 | 0.50 | 2.23 | 94 | 1.23 | 2.14 | 1.65 |
| | | min | 16 | 89 | 13 | 31 | 1758 | 48 | 0.09 | 0.91 | 24 | 0.31 | 0.97 | 0.51 |
| | | max | 208 | 966 | 42 | 73 | 6678 | 72 | 1.01 | 6.01 | 217 | 3.01 | 7.29 | 4.42 |
| Nx3a (<i>n</i> = 8) | blue-colorless | aver | 50 | 264 | 23 | 115 | 3189 | 52 | 1.11 | 2.68 | 68 | 1.12 | 94 | 2.24 |
| | | min | 35 | 10 | 17 | 5 | 2843 | 47 | 0.10 | 0.51 | 42 | 0.68 | 5.57 | 0.08 |
| | | max | 79 | 598 | 30 | 247 | 3922 | 59 | 5.10 | 4.99 | 88 | 1.37 | 316 | 4.46 |
| Nx3b (<i>n</i> = 15) | blue-colorless | aver | 105 | 1944 | 28 | 71 | 2773 | 62 | 0.50 | 2.23 | 30 | 0.68 | 1.86 | 1.65 |
| | | min | 98 | 454 | 25 | 23 | 2220 | 53 | 0.09 | 0.91 | 16 | 0.34 | 0.97 | 0.41 |
| | | max | 198 | 3222 | 34 | 246 | 3317 | 78 | 1.01 | 6.01 | 50 | 0.93 | 7.29 | 4.42 |
| Nx4 (<i>n</i> = 16) | blue-colorless | aver | 51 | 377 | 21 | 45 | 3828 | 83 | 5.98 | 0.87 | 81 | 1.85 | 41 | 0.57 |
| | | min | 16 | 18 | 9 | 1 | 1812 | 50 | 0.11 | 0.18 | 41 | 0.96 | 3.47 | 0.01 |
| | | max | 117 | 846 | 32 | 111 | 6361 | 184 | 30 | 1.83 | 126 | 4.61 | 189 | 1.38 |
| Nx5a (<i>n</i> = 8) | blue | aver | 5 | 462 | 52 | 262 | 3706 | 87 | 0.20 | 3.64 | 1069 | 24 | 9.17 | 3.04 |
| | | min | 2 | 238 | 43 | 227 | 3301 | 84 | 0.13 | 3.16 | 241 | 6.28 | 4.32 | 2.64 |
| | | max | 14 | 784 | 65 | 339 | 4268 | 90 | 0.24 | 4.48 | 2309 | 47 | 18 | 3.97 |
| Nx5b (<i>n</i> = 12) | pink | aver | 52 | 181 | 20 | 428 | 3096 | 45 | 0.05 | 9.95 | 77 | 1.08 | 24 | 9.52 |
| | | min | 17 | 60 | 14 | 274 | 2138 | 37 | 0.03 | 6 | 34 | 0.36 | 7.13 | 5.61 |
| | | max | 133 | 348 | 43 | 548 | 4716 | 52 | 0.10 | 13 | 208 | 2.07 | 59 | 12 |

Table 4. Other trace elements LA-ICP-MS analyses (ppm) of the Greek corundum crystals.

| Sample | ppm | Be | Na | Si | Ca | Mn | Ni | Zn | Rb | Sr | Zr | Nb | Mo | Sn | Ba | Ta | W | Pb | Th | U |
|-----------------------|------|-------|------|------|------|------|------|------|------|------|------|------|------|------|------|------|------|------|------|------|
| Dr1a (<i>n</i> = 8) | aver | bd | 4.5 | 294 | 175 | 0.19 | 0.26 | 0.04 | 0.05 | 0.13 | 0.02 | 0.03 | 0.01 | 0.18 | 0.45 | 0.01 | 0.04 | 0.02 | 0.01 | 0.01 |
| | min | bd | 1.0 | 185 | 117 | 0.14 | 0.10 | 0.03 | 0.00 | 0.00 | 0.02 | 0.02 | 0.01 | 0.07 | 0.01 | 0.01 | 0.02 | 0.01 | 0.01 | 0.01 |
| | max | bd | 20 | 520 | 282 | 0.20 | 0.47 | 0.08 | 0.37 | 0.59 | 0.03 | 0.04 | 0.01 | 0.47 | 3.15 | 0.01 | 0.12 | 0.02 | 0.01 | 0.01 |
| Dr1b (<i>n</i> = 13) | aver | bd | 236 | 1807 | 780 | bd | 57 | bd | bd | bd | bd | 0.07 | 0.36 | bd | 9.80 | 0.05 | 0.17 | bd | 0.02 | 0.01 |
| | min | bd | 152 | bd | 352 | bd | 32 | bd | bd | bd | bd | 0.03 | 0.09 | bd | 0.39 | 0.01 | 0.11 | bd | 0.01 | 0.01 |
| | max | bd | 323 | 2099 | 1202 | bd | 309 | bd | bd | bd | bd | 0.11 | 1.27 | bd | 47 | 0.14 | 0.29 | bd | 0.02 | 0.01 |
| Dr2 (<i>n</i> = 8) | aver | bd | bd | bd | 1414 | bd | bd | bd | bd | bd | bd | 0.15 | bd | bd | bd | 0.02 | 0.48 | bd | 0.01 | 0.01 |
| | min | bd | bd | bd | 1384 | bd | bd | bd | bd | bd | bd | 0.04 | bd | bd | bd | 0.02 | 0.23 | bd | 0.01 | 0.01 |
| | max | bd | bd | bd | 1444 | bd | bd | bd | bd | bd | bd | 0.21 | bd | bd | bd | 0.02 | 0.73 | bd | 0.01 | 0.01 |
| Go1a (<i>n</i> = 11) | aver | bd | bd | bd | 1748 | bd | bd | bd | bd | bd | bd | 28 | bd | 38 | 0.62 | 1.60 | 68 | 0.73 | 6.98 | 0.32 |
| | min | bd | bd | bd | 1482 | bd | bd | bd | bd | bd | bd | 0.46 | bd | 11 | 0.55 | 0.09 | 1.11 | 0.70 | 2.14 | 0.03 |
| | max | bd | bd | bd | 2014 | bd | bd | bd | bd | bd | bd | 90 | 1.46 | 79 | 0.69 | 4.01 | 311 | 0.76 | 21 | 0.72 |
| Go1b (<i>n</i> = 15) | aver | bd | 492 | bd | 2265 | bd | bd | bd | bd | bd | bd | 8.76 | 0.22 | 16 | 0.52 | 1.64 | 44 | 5.43 | 10 | 0.10 |
| | min | bd | 434 | bd | 1859 | bd | bd | bd | bd | bd | bd | 0.29 | 0.11 | 2.14 | 0.23 | 0.11 | 0.48 | 2.23 | 1.07 | 0.01 |
| | max | bd | 524 | bd | 2491 | bd | bd | bd | bd | bd | bd | 55 | 0.34 | 97 | 0.74 | 11 | 498 | 8.63 | 53 | 0.26 |
| Go5a (<i>n</i> = 8) | aver | 0.2 | 1.3 | 224 | 136 | 0.20 | 0.75 | 0.22 | 0.01 | 0.04 | 0.02 | 0.11 | 0.01 | 27 | 0.02 | 0.02 | 0.16 | 0.06 | 0.40 | 0.01 |
| | min | 0.1 | bd | 14 | 88 | 0.20 | 0.04 | 0.03 | 0.01 | 0.01 | 0.01 | 0.01 | 0.01 | 0.09 | 0.01 | 0.00 | 0.03 | 0.01 | 0.01 | 0.01 |
| | max | 0.5 | 3.3 | 369 | 217 | 0.20 | 2.04 | 0.44 | 0.01 | 0.24 | 0.05 | 0.52 | 0.01 | 213 | 0.06 | 0.04 | 0.46 | 0.34 | 1.17 | 0.03 |
| Go5b (<i>n</i> = 14) | aver | bd | bd | bd | bd | bd | bd | bd | bd | bd | bd | 0.16 | 0.45 | bd | 0.87 | 0.07 | bd | bd | 0.03 | 0.02 |
| | min | bd | bd | bd | bd | bd | bd | bd | bd | bd | bd | 0.16 | 0.33 | bd | 0.57 | 0.06 | bd | bd | 0.01 | 0.01 |
| | max | bd | bd | bd | bd | bd | bd | bd | bd | bd | bd | 0.16 | 0.61 | bd | 1.17 | 0.08 | bd | bd | 0.06 | 0.05 |
| Ik1a (<i>n</i> = 8) | aver | 0.45 | 116 | 2479 | 1700 | 0.44 | 0.56 | 2.25 | 0.16 | 1.45 | 0.07 | 2.56 | 0.01 | 4.97 | 0.35 | 0.96 | 1.19 | 2.95 | 1.74 | 0.12 |
| | min | 0.10 | 24 | 353 | 312 | 0.23 | 0.37 | 0.94 | 0.02 | 0.30 | 0.04 | 1.59 | 0.01 | 3.23 | 0.11 | 0.34 | 0.79 | 1.40 | 0.85 | 0.04 |
| | max | 0.70 | 313 | 6492 | 4158 | 1.05 | 0.81 | 4.30 | 0.48 | 3.39 | 0.11 | 4.03 | 0.01 | 7.66 | 0.71 | 1.73 | 1.89 | 4.85 | 2.45 | 0.23 |
| Ik1b (<i>n</i> = 16) | aver | bd | bd | bd | bd | bd | bd | bd | bd | bd | bd | 7.92 | 0.34 | 6.88 | 1.74 | 0.39 | 4.64 | bd | 4.34 | 0.04 |
| | min | bd | bd | bd | bd | bd | bd | bd | bd | bd | bd | 0.40 | 0.11 | 2.83 | 1.13 | 0.10 | 0.74 | bd | 0.04 | 0.01 |
| | max | bd | bd | bd | bd | bd | bd | bd | bd | bd | bd | 37 | 0.84 | 23 | 2.34 | 1.06 | 12 | bd | 31 | 0.22 |
| Nx1a (<i>n</i> = 8) | aver | 2.08 | 5.30 | 543 | 14 | 0.20 | 1.10 | 0.03 | 0.03 | 0.66 | 0.05 | 1.16 | 0.01 | 32 | 0.39 | 15 | 2.74 | 0.02 | 0.40 | 0.01 |
| | min | 0.18 | 1.00 | 399 | 14 | 0.20 | 0.79 | 0.03 | 0.00 | 0.01 | 0.00 | 0.11 | 0.01 | 5.61 | 0.01 | 3.82 | 0.16 | 0.02 | 0.01 | 0.01 |
| | max | 11.03 | 34 | 1110 | 14 | 0.20 | 1.65 | 0.03 | 0.18 | 4.75 | 0.15 | 3.89 | 0.01 | 108 | 3.01 | 46 | 8.74 | 0.02 | 2.45 | 0.02 |
| Nx1b (<i>n</i> = 14) | aver | 2.91 | 205 | 2303 | 1551 | bd | bd | bd | bd | bd | bd | 7.77 | 0.24 | 1040 | 0.11 | 0.39 | 43 | bd | 0.72 | 0.01 |
| | min | 1.31 | 141 | 2069 | 1351 | bd | bd | bd | bd | bd | bd | 0.41 | 0.12 | 166 | 0.10 | 0.16 | 4.04 | bd | 0.02 | 0.01 |
| | max | 4.50 | 253 | 2537 | 1874 | bd | bd | bd | bd | bd | bd | 19 | 0.49 | 1712 | 0.12 | 0.65 | 147 | bd | 2.57 | 0.02 |
| Nx2a (<i>n</i> = 8) | aver | 1.21 | 36 | 804 | 120 | 0.21 | 0.71 | 0.03 | 0.20 | 1.73 | 1.23 | 9.87 | 0.01 | 566 | 0.05 | 1.58 | 105 | 0.02 | 0.13 | 0.01 |
| | min | 0.10 | 1 | 466 | 14 | 0.11 | 0.35 | 0.03 | 0.01 | 0.01 | 0.76 | 0.23 | 0.01 | 197 | 0.01 | 0.18 | 0.63 | 0.02 | 0.01 | 0.01 |
| | max | 3.62 | 271 | 2209 | 648 | 0.35 | 1.39 | 0.03 | 0.04 | 11 | 2.25 | 36 | 0.01 | 887 | 0.17 | 7.14 | 480 | 0.02 | 0.48 | 0.03 |

Table 4. Cont.

| Sample | ppm | Be | Na | Si | Ca | Mn | Ni | Zn | Rb | Sr | Zr | Nb | Mo | Sn | Ba | Ta | W | Pb | Th | U |
|-----------------------|------|------|------|------|------|------|------|------|------|------|------|------|------|------|------|------|------|------|------|------|
| Nx2b (<i>n</i> = 22) | aver | 3.53 | 112 | 1998 | 2118 | bd | bd | bd | 0.92 | 0.88 | bd | 12 | 0.33 | 608 | bd | 3.12 | 147 | 0.53 | 1.48 | 0.08 |
| | min | 2.71 | 90 | 1848 | 1844 | bd | bd | bd | 0.66 | 0.68 | bd | 0.11 | 0.09 | 5 | bd | 0.18 | 1.08 | 0.51 | 0.01 | 0.01 |
| | max | 5.64 | 141 | 2252 | 2418 | bd | bd | bd | 1.25 | 1.15 | bd | 117 | 0.68 | 1842 | bd | 18 | 877 | 0.56 | 13 | 0.49 |
| Nx3a (<i>n</i> = 8) | aver | 2.79 | 1.58 | 501 | 14 | 0.20 | 1.06 | 0.03 | 0.02 | 0.22 | 0.83 | 7.71 | 0.01 | 340 | 0.27 | 2.16 | 100 | 0.02 | 0.07 | 0.01 |
| | min | 0.25 | 1.00 | 412 | 14 | 0.20 | 0.59 | 0.03 | 0.01 | 0.01 | 0.01 | 0.98 | 0.01 | 4.95 | 0.01 | 0.53 | 11 | 0.02 | 0.01 | 0.00 |
| | max | 17 | 5.65 | 693 | 14 | 0.20 | 1.67 | 0.03 | 0.11 | 1.56 | 1.64 | 36 | 0.01 | 574 | 2.05 | 6.02 | 424 | 0.02 | 0.21 | 0.01 |
| Nx3b (<i>n</i> = 15) | aver | 4.25 | bd | bd | bd | bd | bd | bd | bd | bd | bd | 9.87 | 0.23 | 560 | 0.17 | 4.85 | 49 | bd | 3.36 | 0.02 |
| | min | 3.28 | bd | bd | bd | bd | bd | bd | bd | bd | bd | 0.16 | 0.12 | 198 | 0.12 | 0.34 | 0.49 | bd | 0.04 | 0.01 |
| | max | 5.82 | bd | bd | bd | bd | bd | bd | bd | bd | bd | 48 | 0.34 | 947 | 0.22 | 13 | 245 | bd | 20 | 0.08 |
| Nx4 (<i>n</i> = 16) | aver | 7.05 | 1.69 | 500 | 14 | 0.23 | 0.83 | 0.03 | 0.01 | 0.02 | 1.80 | 112 | 0.01 | 244 | 0.06 | 111 | 34 | 0.03 | 0.83 | 0.06 |
| | min | 0.10 | 1.00 | 267 | 14 | 0.15 | 0.28 | 0.03 | 0.00 | 0.00 | 0.01 | 1.16 | 0.01 | 9.19 | 0.01 | 0.31 | 1.75 | 0.02 | 0.01 | 0.01 |
| | max | 38 | 12 | 920 | 14 | 0.61 | 1.92 | 0.03 | 0.17 | 0.12 | 7.56 | 769 | 0.01 | 684 | 0.38 | 549 | 157 | 0.10 | 4.69 | 0.55 |
| Nx5a (<i>n</i> = 8) | aver | 1.12 | 1.12 | 372 | 163 | 16 | 1.17 | 0.79 | 0.01 | 0.04 | 0.06 | 1.53 | 0.01 | 3.64 | 0.66 | 0.23 | 6.70 | 1.80 | 7.40 | 0.02 |
| | min | 0.10 | 1.00 | 328 | 98 | 0.20 | 0.70 | 0.22 | 0.01 | 0.01 | 0.02 | 1.14 | 0.01 | 2.31 | 0.07 | 0.11 | 3.80 | 0.18 | 4.20 | 0.01 |
| | max | 1.86 | 1.99 | 415 | 239 | 110 | 1.89 | 2.25 | 0.01 | 0.08 | 0.10 | 1.91 | 0.01 | 5.45 | 2.75 | 0.35 | 9.45 | 7.72 | 10 | 0.03 |
| Nx5b (<i>n</i> = 12) | aver | bd | bd | bd | bd | bd | bd | bd | bd | bd | bd | 1.49 | 0.63 | 4.30 | bd | 12 | 6.28 | 0.67 | 0.02 | 0.01 |
| | min | bd | bd | bd | bd | bd | bd | bd | bd | bd | bd | 0.10 | 0.28 | 3.22 | bd | 0.19 | bd | 0.49 | 0.01 | 0.01 |
| | max | bd | bd | bd | bd | bd | bd | bd | bd | bd | bd | 2.89 | 0.97 | 6.60 | bd | 96 | 13.1 | 1.03 | 0.02 | 0.01 |

Colored (colorless to blue, pink) sapphires from Gorgona/Xanthi display significant differences regarding the concentration of some chromophore elements. Colorless to blue sapphires are mostly characterized by significant variations of their Ti content which reflects their zoned coloration. Bluish areas display high Ti values, which are up to 6 times higher compared to colorless/white areas and reach up to 6462 ppm. Iron content is quite fixed in both colorless and blue areas, reaching up to 1339 ppm, but is slightly higher in the pink varieties (up to 1782 ppm). Pink sapphires are also characterized by much less Ti (up to 810 ppm) and significantly higher Cr (up to 1082 ppm) concentrations, compared to the colorless/blue areas where Cr values are generally less than 298 ppm. Vanadium and Ga content remains relatively fixed, regardless of the color, with maximum values of up to 227 and 121 ppm, respectively. Mg values are generally higher in the colorless to blue grains, with values up to 536 ppm, while in the pink grains is generally below 65 ppm. Si and Ca display values up to 369 and 217 ppm, respectively, while other elements, are generally close to or below the detection limit, with the exception of Sn and Ta, which reach up to 213 and 4 ppm, respectively, in the colorless to blue grains.

Iron is the most abundant trace element in analyzed sapphires from Ikaria island, with values reaching up to 7324 ppm. Ti displays high values as well, up to 4508 ppm. Cr, Mg and V values are relatively constant with maximum values reaching up to 313, 54 and 164 ppm, respectively. Gallium shows elevated concentrations, up to 114 ppm, resulting in very high values of the Ga/Mg critical ratio. Si and Ca display wide variations between 353–6492 ppm and 312–4158 ppm, with the highest values correlating and thus indicating submicroscopic silicate inclusions (possibly margarite). Other trace elements display generally low concentrations except for Sn, whose values reach up to 23 ppm.

Corundums from Naxos island are mostly characterized by high Fe concentrations, which reach up to 6678 ppm. Higher Fe values are related to areas with more intense blue coloration. Ti is considerably lower, reaching values up to 966 ppm, with the exception of one colorless to blue corundum, where higher values were detected, up to 3222 ppm. Chromium varies significantly, between 1 and 851 ppm. The higher Cr values characterize corundum grains with pink and purple hues. Mg and Ga values range between 2–208 ppm and 42–184 ppm, respectively. The higher Ga concentrations are remarked in the metabauxite-hosted sapphires, that accordingly display the highest Ga/Mg ratio values compared to any other Greek corundums (this study). Vanadium content is quite fixed in all samples and varies between 10 and 65 ppm, with the majority of the measured values being in the range of 20–40 ppm. Si and Ca reach values up to 2537 and 2418 ppm, respectively, probably reflecting the presence of submicroscopic inclusions. Sodium is generally low, but in some cases values up to 271 ppm were detected, probably due to submicroscopic inclusions of silicate minerals (plagioclase and/or paragonite). Almost all corundums contain traces of Be, which ranges between 0.10 and 38 ppm. Manganese is generally close to or below detection, but in the case of a corundum from metabauxites reaches up to 110 ppm. Most samples are characterized by high Sn values, which reach up to 1812 ppm, while Nb is also enriched, reaching up to 769 ppm. Finally, Ta reaches up to 549 ppm, while the rest trace elements are mostly below detection (Table 4).

6. Fluid Inclusions

The fluid inclusions (FI) in the studied corundums range in size between <1 μm and 55 μm . Only one type of two-phase vapor-liquid CO_2 (LcarVcar) FI is observed within all samples [79]. (Figure 6a–d,g). They often have an elongated negative crystal shape of the host corundum (Figure 6a,k). They occur as isolated, and based on their similarity in shape and the mode of occurrence, they are considered as primary FI (Figure 6a,c,f,j,k). However, the most significant criterion for identifying primary FI is when they occur along the growth zones of the corundum (Figure 6i), based on the criteria suggested by Bodnar [80].

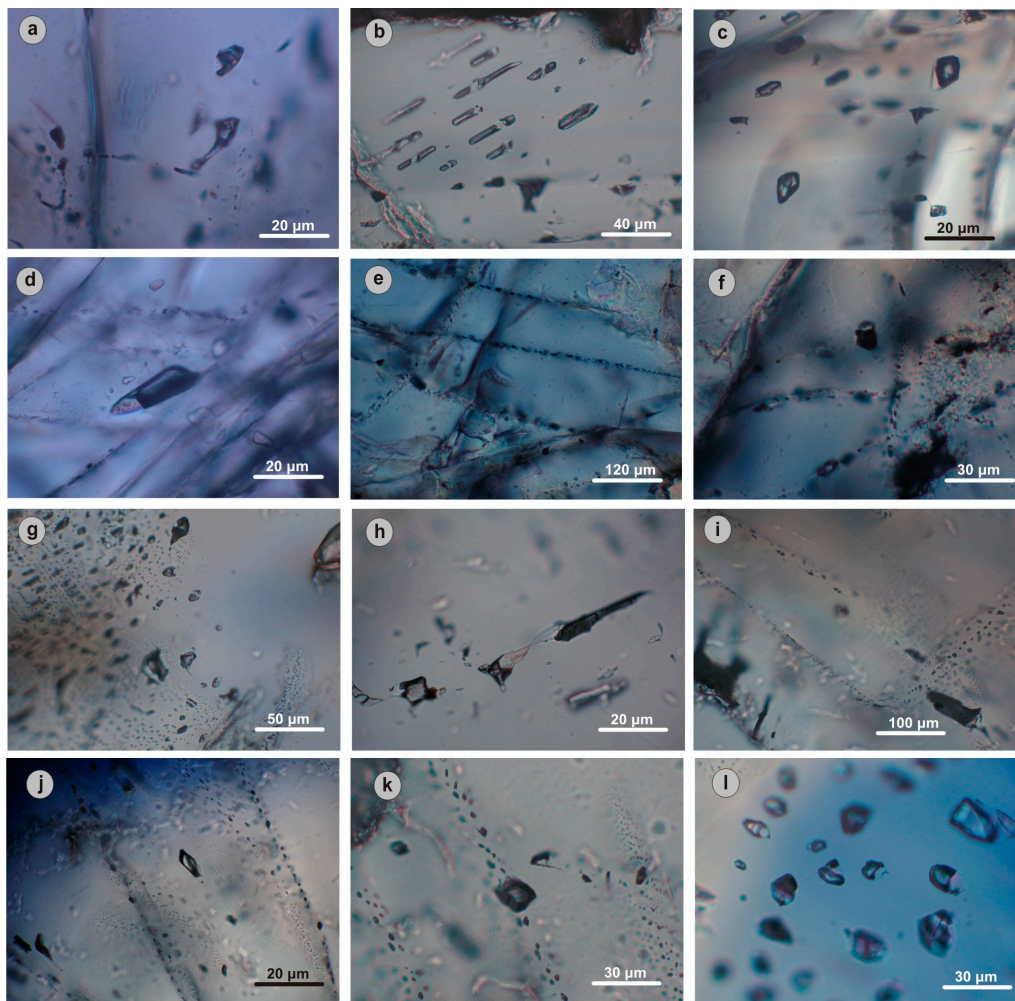


Figure 6. Photomicrographs of FI in corundums from the Rhodope massif of Greece, Paranesti and Gorgona (a–f) and from Naxos island the Attic-Cycladic massif (g–l). (a) Isolated primary two-phase vapor-liquid inclusions composed of $\text{CO}_2 \pm (\text{CH}_4 \text{ and/or } \text{N}_2)$. The fluid inclusion at the upper part has a negative crystal shape, and the inclusion underneath shows necking-down deformation (Drama, thin-section Dr2). (b) Pseudosecondary two-phase carbonic FI along a fracture healed during crystal growth (Xanthi, thin-section Go5a). (c) Primary two-phase carbonic FI (Xanthi, thin-section Go5a). (d) Two-phase carbonic inclusion which shows evidence of post-entrapment modification (brittle crack and halo of neofomed inclusions) (Xanthi, thin-section Go5b). (e) Tiny FI along fracture plane trails, but due to their small size no phases can be identified (Xanthi, thin-section Go1b). (f) Isolated two-phase carbonic inclusion (Xanthi, thin-section Go1b); (g) Oriented cluster of pseudosecondary carbonic FI along fractures healed during crystal growth (thin-section, Nx1a). (h) Isolated primary two-phase carbonic inclusion with necking-down deformation (thin-section, Nx1a). (i) FI along growth zones of the corundum (thin-section, Nx1a). (j,k) Primary two-phase carbonic FI (thin-section, Nx2a). (l) Pseudosecondary two-phase carbonic FI along a fracture healed during crystal growth (thin-section, Nx2b).

Oriented clusters of $L_{\text{car}}-V_{\text{car}}$ FI along planes are very common in the studied samples. They are related to micro-cracks and subsequent fractures healed during crystal growth, and therefore are considered as pseudosecondary (Figure 6b,g,l). Numerous tiny FI (length $<2 \mu\text{m}$) along trails are usually observed, but due to their small size, the nature of the present phase(s) cannot be identified (Figure 6e). They are considered as secondary FI. The majority of the FI appears stretched and necked or empty due to leaking phenomena (Figure 6a,d,h). Microthermometric results were based on primary and pseudosecondary inclusions, without necking-down and post-entrapment modification evidence. However, many measurements were unsuccessful due to the black color of the carbonic fluid in the inclusions and the difficulty to observe phase changes [79].

Table 5 presents the microthermometric data of all studied FI from Drama, Xanthi, Ikaria and Naxos. The melting temperatures of CO_2 (T_{mCO_2}) range between -57.3 and -56.6 °C, at or slightly lower than the triple point of CO_2 (-56.6 °C). This indicates that the fluid is dominated by CO_2 with very small quantities of CH_4 and/or N_2 . Temperatures of T_{m} were not obtainable in the sample Dr1a from Paranesti (Drama). Clathrate nucleation was not observed in any measured fluid inclusion, demonstrating that liquid water (H_2O) was not incorporated in the whole process of the corundums formation. All FI homogenized to the liquid carbonic phase (LCO_2) at temperatures (T_{hCO_2}) varying from 27.3 to 31.0 °C. This T_{h} is close to the critical temperature of pure CO_2 and corresponds to densities of the source fluids from 0.46 to 0.67 g/cm^3 . Figure 7 shows the histograms of the T_{hCO_2} of the FI from the four different studied corundum occurrences in Greece (Paranesti, Gorgona, Naxos, Ikaria).

Table 5. Microthermometric data of studied primary and pseudosecondary fluid inclusions from corundum crystals in Greece.

| Sample | Locality | <i>n</i> | $T_{\text{m CO}_2}$ (°C) | $T_{\text{h CO}_2}$ (°C) | Densities (g/cm^3) |
|--------|---------------------|----------|--------------------------|--------------------------|-------------------------------|
| Dr1a | Paranesti, Drama | 7 | -57.2 to -56.7 | 28.7 – 31.1 | 0.46 – 0.64 |
| Dr2 | | 7 | -57.1 to -56.6 | 27.4 – 30.4 | 0.57 – 0.67 |
| Go1a | Gorgona, Xanthi | 4 | -57.0 to -56.8 | 29.2 – 30.2 | 0.58 – 0.62 |
| Go1b | | 3 | -56.7 to -56.6 | 27.8 – 30.5 | 0.57 – 0.66 |
| Go5a | | 6 | -57.2 to -56.8 | 28.2 – 30.9 | 0.53 – 0.65 |
| Go5b | | 6 | -57.2 to -56.7 | 27.4 – 29.2 | 0.62 – 0.67 |
| Ik1a | Ikaria | 3 | -56.9 to -56.6 | 30.1 – 30.8 | 0.54 – 0.59 |
| Ik1b | | 6 | -57.0 to -56.6 | 27.4 – 28.3 | 0.65 – 0.67 |
| Nx1a | Naxos | 8 | -57.2 to -56.6 | 27.3 – 31.0 | 0.51 – 0.67 |
| Nx1b | | 10 | -57.3 to -56.7 | 28.1 – 30.5 | 0.57 – 0.65 |
| Nx2a | | 4 | -57.2 to -56.6 | 27.9 – 29.3 | 0.62 – 0.66 |
| Nx2b | | 6 | -57.1 to -56.8 | 28.9 – 31.0 | 0.51 – 0.63 |
| Nx4b | | 4 | -57.2 to -56.9 | 27.5 – 30.4 | 0.57 – 0.67 |

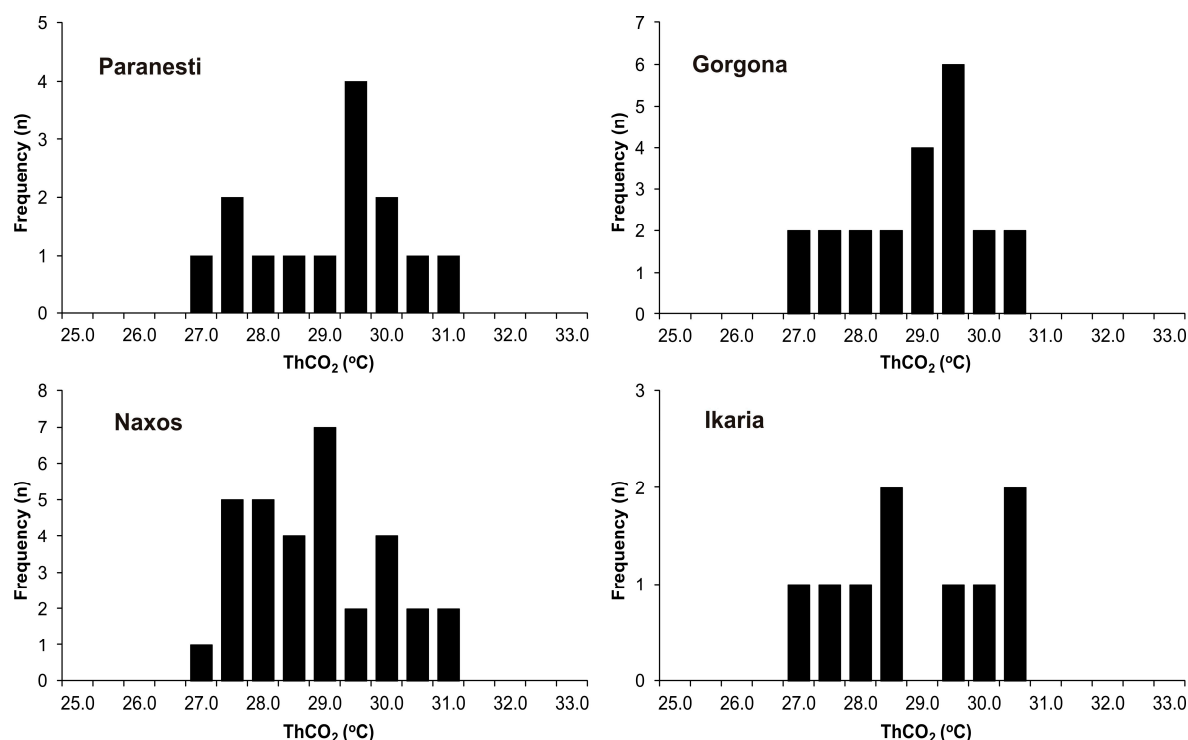


Figure 7. Histograms of homogenization temperatures of CO₂ (ThCO₂) to the liquid phase (LCO₂) in the fluid inclusion from the Rhodope massif (Paranesti, Gorgona) and the Attic-Cycladic massif (Naxos, Ikaria) from Greece.

7. Oxygen Isotope Data

Oxygen isotope compositions (Table 6) confirm their geological typology, i.e., with, respectively, $\delta^{18}\text{O}$ of $4.9 \pm 0.2\text{‰}$ for sapphire in plumasite, 20.5‰ for sapphire in marble and 1‰ for ruby in mafics (Figure 8). The desilicated blue sapphire-bearing pegmatite from Naxos have similar oxygen isotope values to those from desilicated pegmatites in mafic host rocks from elsewhere [2,7,14,81,82]. The O-isotope composition of sapphire is buffered by the $\delta^{18}\text{O}$ value of the mafic host rock. The ruby in pargasite schists from Paranesti has a very low $\delta^{18}\text{O}$ -value of 1‰ that can be interpreted in different ways: (i) inherited pre-metamorphic reactions between sea-water and hot basic/ultrabasic rocks before subduction and metamorphism; (ii) syn-metamorphism depletion in ^{18}O related to hydration during amphibolite facies metamorphic conditions; (iii) post-amphibolite facies metamorphism with recrystallization under the effect of metasomatism of the metamorphosed mafic/ultramafic rocks with a high depletion in ^{18}O ; and (iv) metamorphic/metasomatic conditions involving deeply penetrating meteoric waters along major crustal structures, see Wang et al. [83]. At the moment, the absence of more O-isotope data on this type of ruby precludes any of these possible hypotheses. The two $\delta^{18}\text{O}$ -values of ruby in marble, between 20.5‰ and 22.1‰ , are in agreement with the range of values found for this type of ruby worldwide [2,14].

Table 6. Oxygen isotope values of corundum from Greece. $\delta^{18}\text{O}$ corundum (‰, V-SMOW) (after Wang et al. [83]).

| Sample | $\delta^{18}\text{O}$ | Description |
|--------|-----------------------|---|
| Nx2a | 4.8 | Blue to colorless sapphire in plumasite |
| Nx3a | 5.1 | Blue to colorless sapphire in plumasite |
| Dr1b | 1.0 | Red ruby in pargasite-schist |
| Go5a | 22.1 | Pink-purple sapphire in marble |
| Go5b | 20.5 | Pink sapphire in marble |
| Ik1a | 22.4 | Blue sapphire in metabasite |

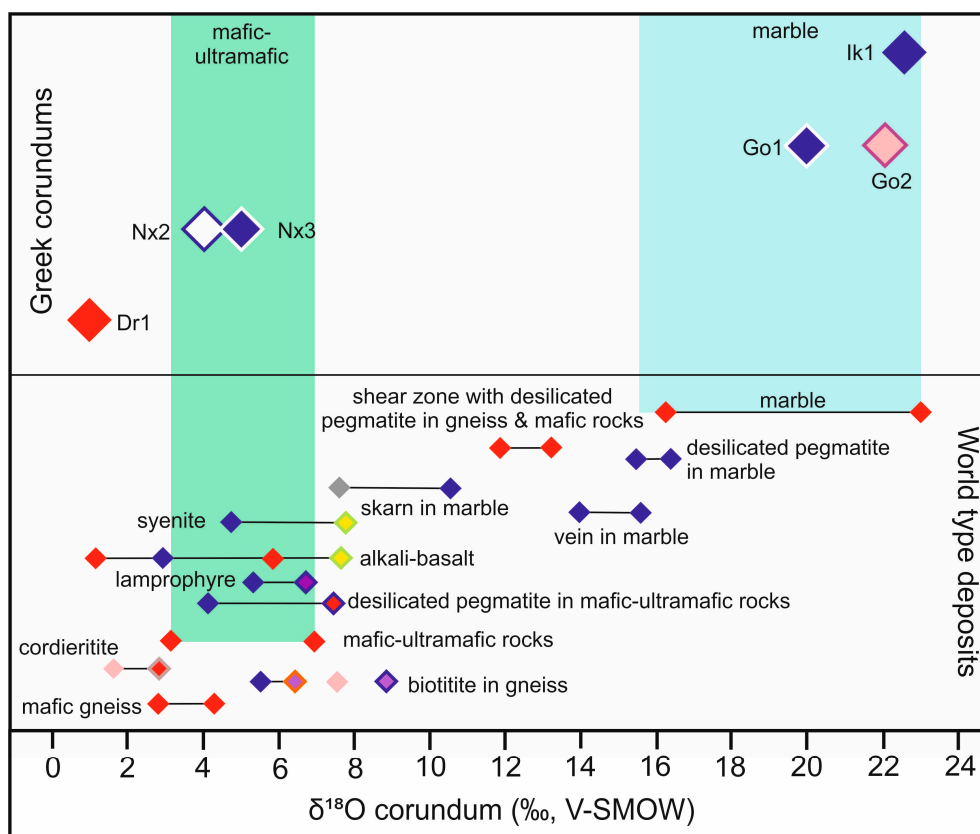


Figure 8. Oxygen isotopic composition of Greek corundum (after Wang et al. [83]) compared with the oxygen isotopic ranges from corundum deposits worldwide from the data of Giuliani et al. [2,7,14,81,82]. Color in diamonds represents the color of the studied corundums. Colorless sapphires are represented by white diamonds.

8. Discussion

8.1. Trace Elements Fingerprint: Metamorphic versus Magmatic Origin of Greek Corundum

Chromophore and genetic indicator elements (Fe, Cr, Ti, V, Ga and Mg) are commonly used to distinguish corundum from different primary sources using elemental diagrams [16,84–88]. In the $(Cr + V)/Ga$ versus Fe/Ti diagram (Figure 9a, [84,85]), displaying the fields for metamorphic and magmatic corundums, the majority of the samples plot in the field of metamorphic corundum, exhibiting a large variation of Fe/Ti ratios. Some sapphires from Naxos island that plot in the magmatic field have very low Cr/Ga ratios. Rubies from Paranesti/Drama show high Cr/Ga and Fe/Ti ratios, followed by the pink and purple sapphires from Naxos island. Both colorless to blue and pink sapphires from Gorgona/Xanthi and blue sapphires from Ikaria island are characterized by relatively fixed Cr/Ga , but display variations with respect to their Fe/Ti ratios.

In the $Fe - Cr \times 10 - Ga \times 100$ discrimination diagram (Figure 9b; after Sutherland et al. [84]), the rubies from Paranesti are extremely rich in Cr_2O_3 and display a linear trend inside the metamorphic corundum field. Sapphires from Gorgona/Xanthi, Naxos and Ikaria islands are scattered in both the metamorphic and magmatic corundum fields. Colored sapphires from Gorgona/Xanthi are scattered in both the metamorphic and magmatic fields and display two trends, along the $Ga-Fe$ and $Ga-Cr$ lines, with the pink varieties plotting closer to the Cr_2O_3 edge, indicating a direct relationship between color and Cr_2O_3 content. Colorless to blue sapphires from Naxos island mostly plot along the $Fe-Ga$ line, in the magmatic corundum field, while the pink and purple varieties display a linear trend towards the Cr_2O_3 edge, inside the metamorphic field, which is subparallel to the trend of pink sapphires from Gorgona/Xanthi. Blue sapphires from Ikaria island clearly plot in the metamorphic field.

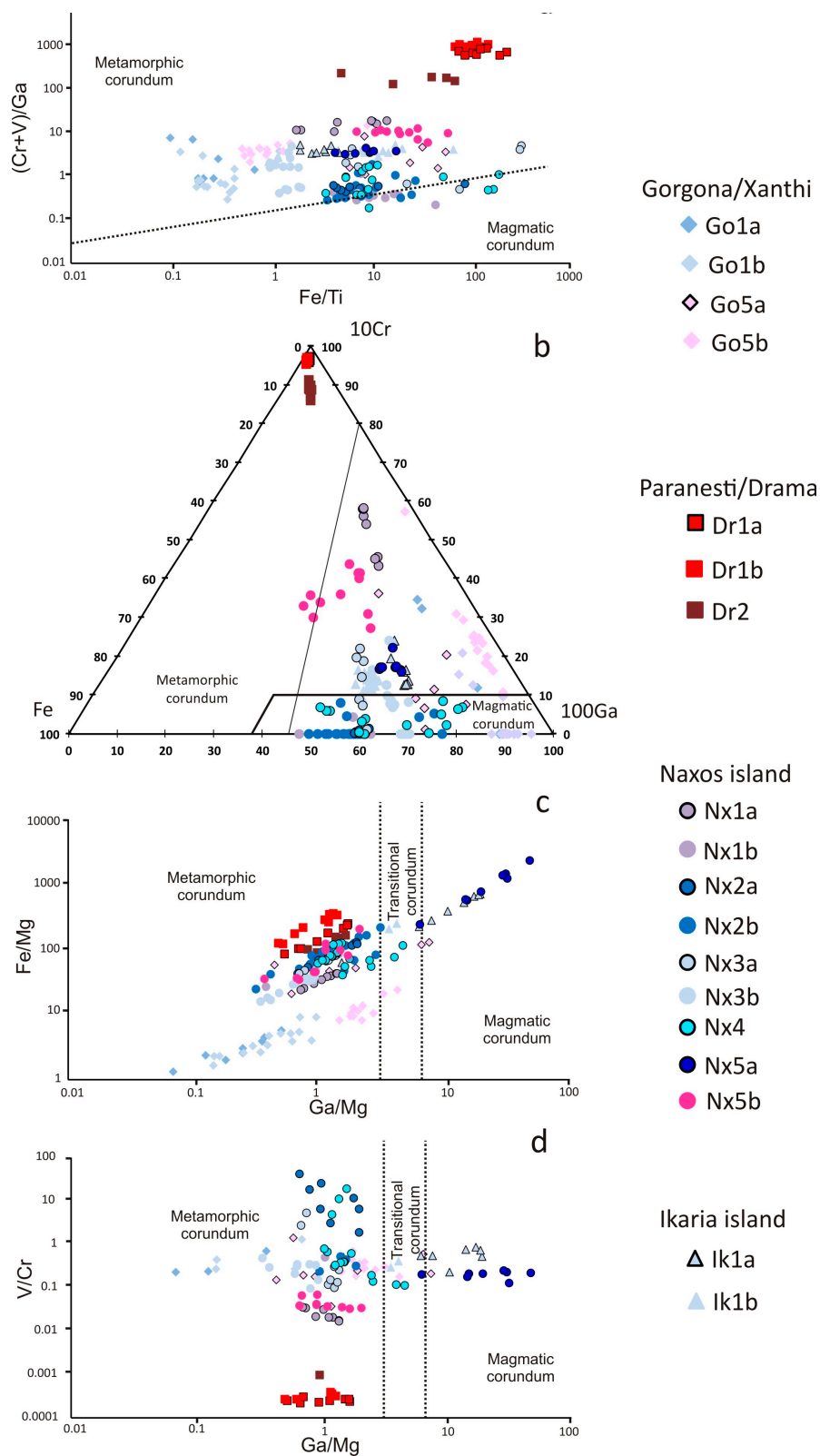


Figure 9. Greek corundum LA-ICP-MS analyses plotted on a (a) $(Cr + V)/Ga$ versus Fe/Ti discrimination diagram separating the fields for magmatic and metamorphic corundums (after Sutherland et al. [84] and Harris et al. [85]); (b) trace element $Fe - Cr \times 10 - Ga \times 100$ discrimination diagram after Sutherland et al. [84]; (c) Fe/Mg versus Ga/Mg diagram discrimination separating the fields for magmatic, transitional and metamorphic corundums (after Peucat et al. [16], Sutherland et al. [84]; (d) V/Cr versus Ga/Mg discrimination diagram separating the fields for magmatic, transitional and metamorphic corundums (after Sutherland et al. [86]).

In the Fe/Mg versus Ga/Mg plot (Figure 9c), most samples plot in the metamorphic corundum field, except for sapphires from metabauxites of Naxos and Ikaria islands and two analyses of pink sapphires from Gorgona/Xanthi. A few blue sapphires from Naxos island and pink sapphires from Gorgona/Xanthi plot in the in-between area of transitional corundum. Two distinct trends can be remarked in the metamorphic corundum field: Sapphires from Gorgona/Xanthi form a linear trend, with the pink varieties exhibiting higher both Fe and Ga concentrations. The rest of the analyzed corundums plot in a relatively small area, parallel to the previous trend, but are also characterized by higher Fe values, the highest of which characterize the rubies from Paranesti/Drama.

The V/Cr versus Ga/Mg diagram is useful for deciphering the genetic environments of corundum (Figure 9d). The majority of the analyzed samples plot in the metamorphic corundum field, with the exception of a few analyses that fit in the transitional field and the metabauxite-hosted sapphires from Ikaria and Naxos islands that have a magmatic signature (Figure 9d). In this diagram, rubies from Paranesti/Drama plot close to the Ga/Mg axis, as they are characterized by very low V content. On the other hand, colored sapphires from the other localities plot in two vertical trends. The first one, is characterized by fixed Ga/Mg content and refers to pink, purple and the majority of the colorless to blue sapphires from Naxos island, and expresses a decrease in the Cr content from the purple to the pink and finally the blue varieties and subsequent increase of their V content. The second trend is characterized by stable V/Cr ratio, but shows a significant variation regarding its Ga/Mg content. Gallium concentration increases by three orders from the blue sapphires of Gorgona/Xanthi towards the pink varieties of the same locality and finally to the metabauxite-hosted sapphires of Ikaria and Naxos islands which show the highest Ga values.

In the $(\text{FeO}-\text{Cr}_2\text{O}_3-\text{MgO}-\text{V}_2\text{O}_3)$ versus $(\text{FeO} + \text{TiO}_2 + \text{Ga}_2\text{O}_3)$ diagram after Giuliani et al. [87,88], which further differentiates the metamorphic environments (Figure 10), all rubies from Paranesti/Drama clearly fall in the field of rubies with mafic/ultramafic origin. Pink sapphires from Gorgona/Xanthi, plot in an overlapping area between the marble-hosted rubies and the metasomatic corundum fields, while the rest of sapphires from this locality, which are colorless to blue in color, plot in a linear trend along the y axis of the diagram, indicating variable contents of Fe, Ti and Ga. The rest of the studied samples (Naxos and Ikaria sapphires) plot mostly in the field of metasomatic corundum, with some analyses plotting in the borders with the field of syenite-related sapphires. In general, the trends observed in Figures 9 and 10 reflect variations in chromophore element concentrations, even in samples from the same locality. This could be attributed to changes in chemistry and physicochemical conditions of the corundum-forming environment, perhaps due to metasomatic processes as described by Harris et al. [85].

8.2. Comparison with Corundum Deposits around the World

Various plots, based on trace element fingerprints, have been proposed as a useful tool for distinguishing the origin and genesis of gem corundum deposits (Figures 11 and 12; [4,16,89–93]).

In the $\text{Mg} \times 100 - \text{Fe} - \text{Ti} \times 10$ diagram (Figure 11a), rubies from Paranesti/Drama plot both in the magmatic and metamorphic fields, and mostly along the Fe–Mg line. Analyses that plot in the magmatic field are also of metamorphic origin and indicate the variation of the Fe/Mg ratio, thus suggesting a limitation of this chemical diagram. Sapphires from Gorgona/Xanthi and the majority of the Naxos island's sapphires plot in the metamorphic field. The blue and pink sapphires from Gorgona/Xanthi, as well as some blue sapphires from Naxos island, plot along the Mg–Ti line of low-Fe metamorphic sapphires (e.g., Ilakaka/Madagascar and Ratnapura Balangoda/Sri Lanka), subparallel to the so-called Kashmir trend. Other colored sapphires from Naxos plot subparallel to the Kashmir trend of metasomatic blue sapphires, but they are characterized by elevated contents of Fe in the purple- and Mg in the pink-colored varieties, and are scattered through the Bo Phloi/Thailand atypical blue sapphires. Metabauxite-hosted sapphires from Naxos and Ikaria islands display a Ti-rich magmatic trend and plot preferably along the Fe–Ti line and follow the Fe–Ti Pailin (Cambodia) of magmatic blue sapphires.

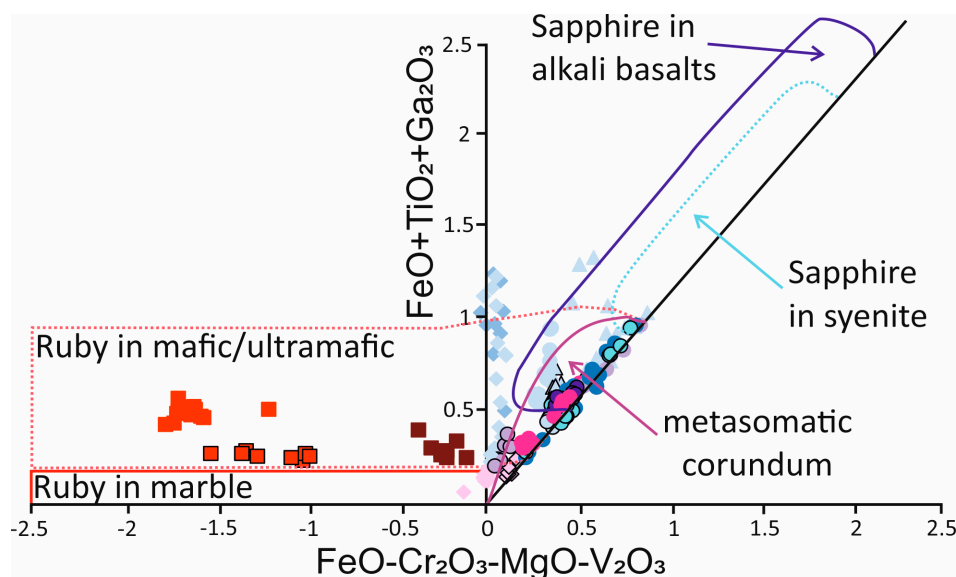


Figure 10. Greek corundum LA-ICP-MS analyses plotted on a $\text{FeO}-\text{Cr}_2\text{O}_3-\text{MgO}-\text{V}_2\text{O}_3$ versus $\text{FeO} + \text{TiO}_2 + \text{Ga}_2\text{O}_3$ discrimination diagram after Giuliani et al. [87,88]. Symbols as in Figure 9.

In the $\text{Fe} \times 0.1 - (\text{Cr} + \text{V}) \times 10 - \text{Ti}$ plot, after Peucat et al. [16], rubies from Paranesti/Drama, as well as pink and purple sapphires plot close to the $\text{Cr} + \text{V}$ edge, as they are enriched in Cr (Figure 11b). Moreover, pink sapphires from Gorgona/Xanthi, along with metabauxite-hosted sapphires from Ikaria and Naxos islands, plot close to the same edge, but due to their relative enrichment in V, rather than Cr. The blue sapphires from Gorgona/Xanthi, along with some blue sapphires from Naxos, plot close to the Ti edge, in a linear array parallel to the $(\text{Cr} + \text{V})-\text{Ti}$ line. Sapphires from Naxos are scarce in the diagram, mainly reflecting their variable content of Ti, with the weak-colored areas plotting close to or along the $\text{Fe}-(\text{Cr} + \text{V})$ line. The majority of the Naxos sapphires form a linear array, parallel to the Mogok marble-hosted trend, but they differ in respect to their lower Fe and higher $\text{Cr} + \text{V}$ contents. Some Naxos sapphires plot close to the fields for Colombia and Umba blue sapphires hosted in desilicated pegmatites.

In the Fe versus Ga/Mg diagram (Figure 12a; after Peucat et al. [16], Zwaan et al. [89]), the majority of the analyzed corundums are scattered in the field of metamorphic sapphires, and specifically in the plumasitic sub-field. Some sapphires from Naxos island, with blue and pink color plot in the field of alluvial sapphires from Yogo Culch Montana, while blue sapphires from Gorgona/Xanthi are characterized by very low Ga/Mg ratios and thus plot slightly outside the metamorphic field. Metabauxite-hosted sapphires from Naxos and Ikaria islands plot along the Main Asian Field (MAF) of sapphires related to alkali basalt. They form a linear array indicating variations in their Ga/Mg ratio and their Fe content is slightly higher compared to sapphires from Pailin (Cambodia) and Ilmen (Russia). Finally, a few analyses of pink sapphires from Gorgona/Xanthi are plotted in the MAF field, and are characterized by slightly higher both Fe and Ga/Mg values, compared to the rest pink and colorless to blue sapphires of this location.

The Cr_2O_3 versus Fe_2O_3 diagram (Figure 12b), adapted from Schwarz et al. [90], shows different types of African deposits: marble-type from Mong Hsu and Mogok (Myanmar), desilicated pegmatite from Mangari (Kenya), amphibolitic-type from Chimwadzulu (Malawi), Songea and Winza (Tanzania) and basaltic-type from Thai (Thailand-Cambodia border region). The majority of the Paranesti/Drama rubies plot outside the fields of rubies from elsewhere, because they contain significantly more Cr_2O_3 . Some samples, though, poorer in Cr_2O_3 , fit well into the Winza (Tanzania) ruby field. Sapphire samples plot mostly along the Fe_2O_3 axis, with the majority of the compositions being comparable with colored sapphires from Winza.

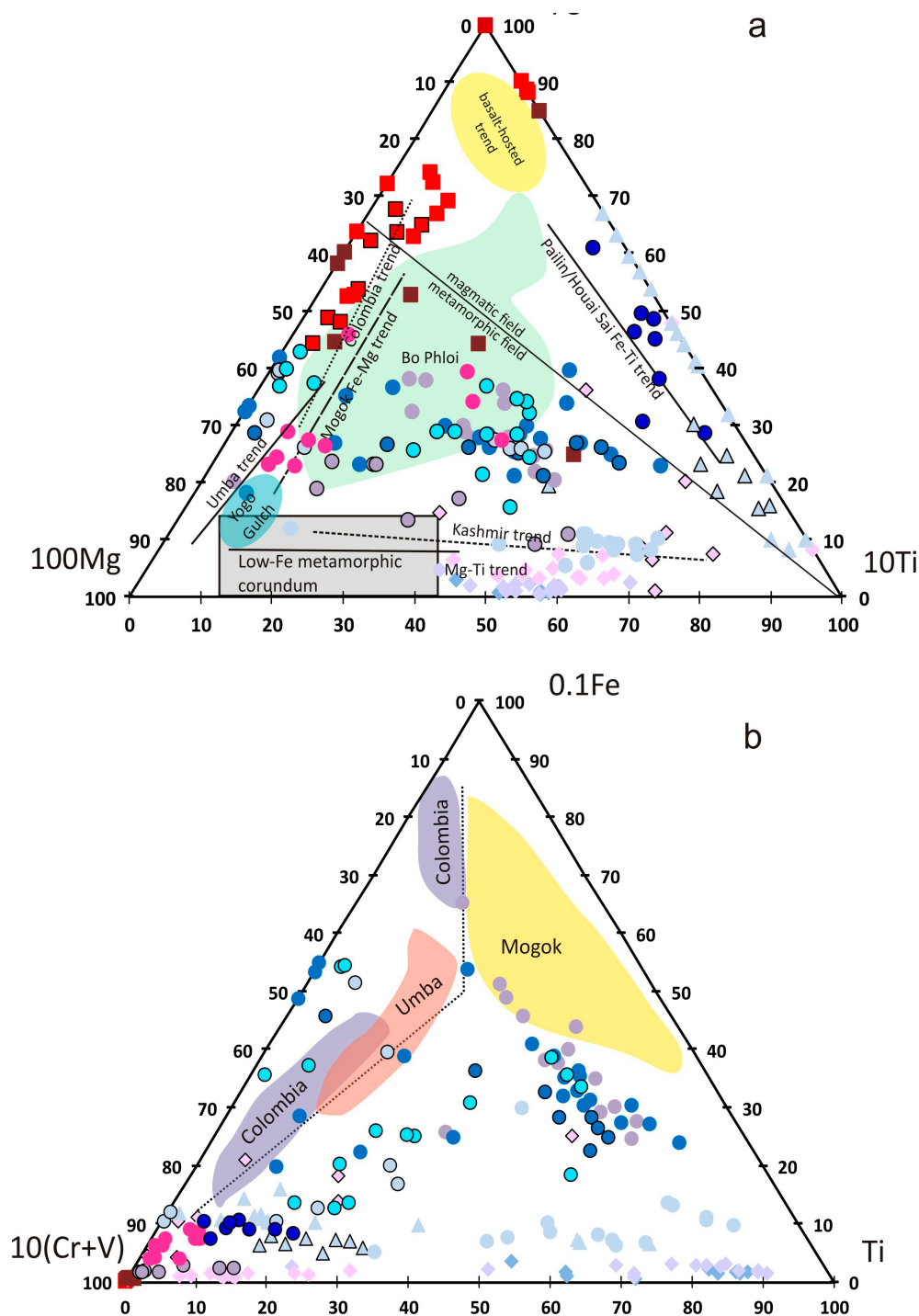


Figure 11. Greek corundum LA-ICP-MS analyses plotted on a (a) $\text{Mg} \times 100 - \text{Fe} - \text{Ti} \times 10$ discrimination diagram. Also shown are the metamorphic Fe–Mg and Fe–Ti trends of Mogok and low-Fe sapphires of Pailin, Ilakaka and Ratnapura Balangoda, the Umba and Kashmir trends of metasomatic blue sapphires, and the Bo Phloi scattering of atypical blue sapphires (modified after Peucat et al. [16]); (b) $\text{Fe} \times 0.1 - (\text{Cr} + \text{V}) \times 10 - \text{Ti}$ diagram for Colombia, Mogok and Umba blue sapphires along with the plots from the Greek corundums, modified after Peucat et al. [16]. Symbols as in Figure 9.

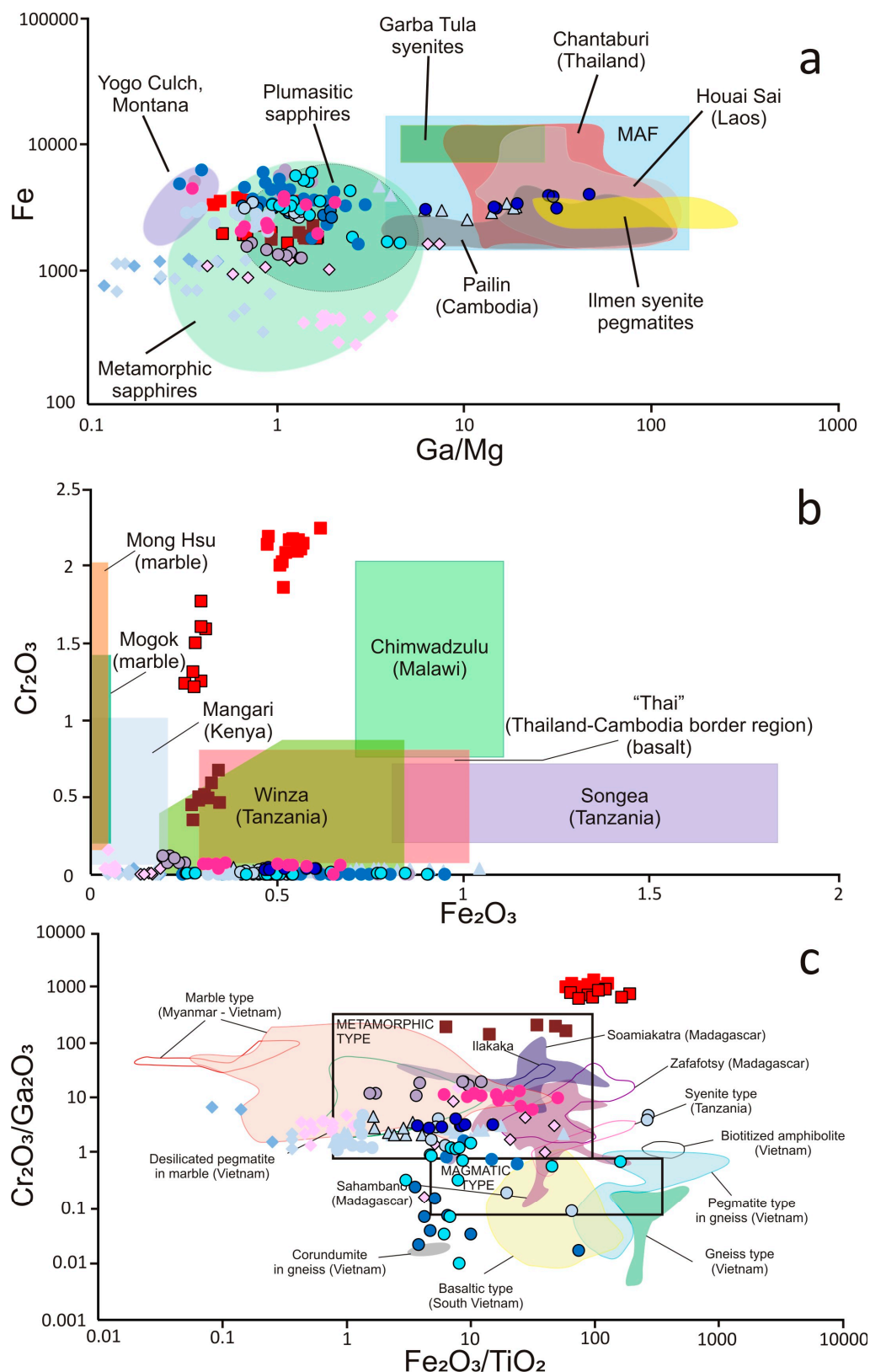


Figure 12. Greek corundum LA-ICP-MS analyses plotted on a (a) Fe versus Ga/Mg discrimination diagram (after Peucat et al. [16], Zwaan et al. [89]); (b) Cr_2O_3 versus Fe_2O_3 diagram demonstrating the fields of different African deposits (modified after Schwarz et al. [90]); (c) $\text{Cr}_2\text{O}_3/\text{Ga}_2\text{O}_3$ versus $\text{Fe}_2\text{O}_3/\text{TiO}_2$ plot demonstrating composition of diverse corundum deposits (modified after Rakotondrazafy et al. [91], Sutherland et al. [4], Pham Van et al. [92], Simonet et al. [93]). Symbols as in Figure 9.

The $\text{Cr}_2\text{O}_3/\text{Ga}_2\text{O}_3$ versus $\text{Fe}_2\text{O}_3/\text{TiO}_2$ diagram (Figure 12c; modified from Rakotondrazafy et al. [91]), displays the geochemical fingerprint of corundums from different types. The majority of analyzed corundums plot in the field of metamorphic origin. It is clear that rubies from Paranesti/Drama show higher Cr_2O_3 values, and thus cannot plot in fields of rubies from elsewhere.

Some rubies from Paranesti also fall close to the Soamiakatra rubies, which are hosted in clinopyroxenite enclaves of alkali basalts. Pink and purple sapphires from Naxos island display variation of their $\text{Fe}_2\text{O}_3/\text{TiO}_2$ ratio. The pink sapphires plot in a common field of the Soamiakatra and Sahambano sapphires (Madagascar), while the purple varieties are scattered in a sector overlapping both the marble- and the desilicated pegmatite in marble-types of Vietnam.

Colorless to blue sapphires from Naxos plumasites are scattered along the lower limit of the metamorphic field, indicating significant variation of their $\text{Fe}_2\text{O}_3/\text{TiO}_2$ values, while the $\text{Cr}_2\text{O}_3/\text{Ga}_2\text{O}_3$ values stay relatively fixed. Pink-colored sapphires from Gorgona/Xanthi plot partly inside the marble-hosted corundum from Vietnam, while the blue varieties plot in the extension of this trend, slightly outside the field, indicating minor Fe_2O_3 content. Metabauxite-hosted corundum from Naxos island plot slightly outside the magmatic corundum field, and their ratios are not comparable with any other corundum of the plot, except a few analyses, which plot close to the Vietnamese field of gneiss-hosted corundumite. Ikaria metabauxite-hosted samples plot well into the metamorphic corundum field and show a wide range of $\text{Fe}_2\text{O}_3/\text{TiO}_2$ values, covering the fields between marble-hosted and desilicated pegmatite in marbles (Vietnam), Sahambano and Zafafotsy (Madagascar) corundum deposits.

8.3. Fluid Characterization

The fluid inclusions study in the corundum (rubies and sapphires) from the four Greek occurrences revealed the presence of CO_2 -dominated fluids with very small quantities of CH_4 and/or N_2 , and relatively low densities, varying between 0.46 and 0.67 g/cm³ [79]. Primary and pseudosecondary water-free carbonic fluid inclusions represent the main fluid, which was incorporated during the crystallization of rubies and sapphires. The absence of any significant change in the fluid composition and density of the primary and pseudosecondary inclusions possibly suggests that (i) the fluid was homogeneous and related to the same source; and (ii) the host rocks were not affected by the circulation of any external fluids. The CO_2 -rich fluids are likely of metamorphic origin and probably derived from devolatilization of marble in most cases (Naxos and Ikaria).

Most of the corundum in different geological environments worldwide generally contains pure or nearly pure CO_2 -bearing fluid inclusions. Previous studies have shown that in metamorphic complexes, CO_2 -bearing fluids were incorporated in the corundum formation from granulite facies rocks in Sri Lanka [94], in the marble hosted ruby deposits from Luc Yen in North Vietnam [95] and in pegmatoids from the Nestos Shear Zone in Greece [57]. Corundum occurrences with pure or almost pure CO_2 -bearing fluids, without any water included, were documented in sapphires from pegmatites in the Kerala district of India [96] and in a corundum bearing skarn from granulites in Southeast Madagascar [97]. In other corundum occurrences, such as in the Kashmir blue sapphires and in the Thailand sapphires, CO_2 is an important component of the source fluids [98,99]. The occurrence of high-density CO_2 -rich fluid inclusions in granulite facies rocks shows that large amounts of CO_2 infiltrate the lower crust during the peak of metamorphism [100–102]. However, Hollister et al. [103] have shown that low-density CO_2 fluid inclusions must have been trapped after the peak of metamorphism. Two main sources for input of CO_2 fluids in the lower crust have been suggested [101,104,105]: from the mantle, or from the metamorphism of previously dehydrated crust. High-Al and low-Si protoliths in a high regional metamorphic grade can produce a pure supercritical CO_2 fluid and lead to the formation of corundum. A mantle-derived CO_2 has been suggested for Naxos by Schuiling and Kreulen [106].

In the present study, similar fluids containing almost pure CO_2 have been documented. Water was not identified in the fluid inclusions, neither by optical microscopy nor by any phase transition during

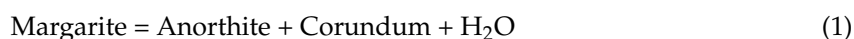
microthermometry. This excludes the possibility of fluid immiscibility for the corundum formation and implies the presence of a primary water-free (or very poor) CO₂ dominated fluid. However, the presence of minor amounts of water in the paleofluid in all studied corundums cannot be excluded, due to the presence of hydrous mineral inclusions in the corundum. Already, Buick and Holland [107] have argued that the “primary” fluid inclusions in the metamorphic complex of Naxos have been compositionally modified by selective leakage of H₂O during uplift, and Krenn et al. [57] reported on recrystallization-induced leakage resulting in minor admixture of H₂O from former hydrous inclusions in corundum from pegmatites along the Nestos suture zone, Xanthi area.

It is very likely that the studied primary low-density fluid inclusions ($d = 0.46\text{--}0.67\text{ g/cm}^3$) were entrapped after the peak of metamorphism, suggesting that corundum formation took place during retrogression. The pseudosecondary, also low-density, carbonic fluid inclusions were entrapped in trails during the corundums formation process and are related to the evolution of the metamorphic events at a retrograde metamorphic regime of cooling and uplift and the subsequent exhumation, also after the peak of metamorphism. These variations in the density of the fluid inclusions can be interpreted as the result of pressure variation associated with successive localized microfracturing, a process which was suggested in the case of Luc Yen rubies of North Vietnam [95]. However, a continuous entrapment of the carbonic fluids during growth of corundum with pressure decreasing is not excluded.

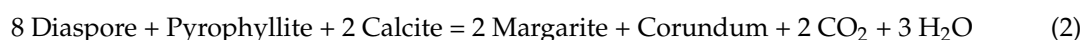
8.4. Conditions of Greek Corundum Formation

The Xanthi and Paranesti corundums belong to metamorphic s.s. deposits, according to the classification of Giuliani et al. [2,7] and Simonet et al. [3], and more specifically, to those related to meta-limestones and mafic granulites, respectively. Both occurrences formed during the retrograde metamorphic path of high-temperature/medium-pressure metamorphism of platform carbonates and amphibolites during the Cenozoic collision that resulted in the Nestos Suture Zone. Wang et al. [30] concluded that Paranesti rubies were formed within an ultramafic precursor, most probably an aluminous clinopyroxenite, during amphibolite facies metamorphism. The estimated P–T conditions for their formation are $4\text{ kbar} < P < 7\text{ kbar}$ and $580\text{ }^{\circ}\text{C} < T < 750\text{ }^{\circ}\text{C}$, and with subsequent retrogression.

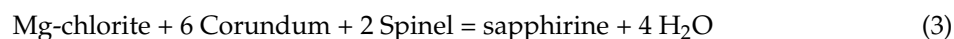
The Paranesti (and Gorgona/Xanthi) corundum-bearing assemblages followed a nearly isothermal decompression within the amphibolite facies and then a further evolution towards the greenschist facies, along the path that was proposed by Krenn et al. [57] for the Nestos suture zone (Figure 13). This path records a transition from the kyanite to the sillimanite stability field during retrogression, as observed by former kyanite surrounded by fibrolitic sillimanite ([57,108] and this study). In the studied samples from Paranesti, corundum surrounds kyanite, and was probably formed after kyanite in the stability field of sillimanite during the retrogression. Mineralogical observations of the corundums from Paranesti ([30] and this study) indicate that the margarite occurs as reaction rims around ruby grains, suggesting that it was formed subsequently due to retrogression and according to the following reaction:



In contrast to Paranesti, margarite in the Gorgona/Xanthi corundum-bearing marbles seems to be a prograde mineral ([22,109] and this study), indicating that corundum along with anorthite could have been formed by the breakdown of margarite (see Reaction (1)). In the studied samples, margarite is either in contact or is separated from corundum by a kaolinite rim, which probably represents earlier anorthite. As described by Storre and Nitsch [110] and Chatterjee [111,112], margarite breakdown to anorthite and corundum takes place at temperatures of 610, 625 and 650 °C for pressures of 6, 7 and 8 kbar, respectively. On the other hand, and under the assumption that margarite was formed together with corundum, a more complex reaction:



as described by Okrusch et al. [113] and Haas and Holdaway [114] may explain this assemblage. This reaction requires the metastable persistence of diaspore + pyrophyllite, which should have otherwise reacted to form Al-silicate about 40–60 °C below the lower stability limit of corundum [113]. The assemblage corundum and chlorite within the Gorgona marbles can be formed according to the following reaction, as experimentally demonstrated by Seifert [115]:



but the absence of sapphirine in the studied samples indicates that P–T did not exceed 6 kbar for temperatures between 620 and 720 °C [115]. The formation of the Xanthi corundum under dissociation of Mg-spinel + calcite into corundum + dolomite during the retrograde metamorphism of spinel-bearing dolomites according to the reaction:



was not observed, but cannot be ruled out. This reaction path has been described by Buick and Holland [116] in spinel-bearing dolomites from the leucocratic core of Naxos, where spinel crystals are separated from the calcite of the host rock by corundum + dolomite mantles, and they are often surrounded by Mg-chlorite + pargasite. The above authors suggested synchronous formation of Mg-chlorite + pargasite in place of spinel + calcite. Decomposition of spinel into corundum during the retrograde metamorphism in marbles as described by Reaction (4) was described as the major corundum-forming mechanism for the rubies at Jegdalek (Afghanistan), Hunza (Pakistan) and Luc Yen (Vietnam) [117].

In summary, conditions of corundum formation in the Gorgona marbles as suggested by Liati [22,109] and this study, are in accordance to those estimated by Wang et al. [30] for the Paraneesti rubies. As an alternative hypothesis, corundum in the Gorgona marbles could have formed at lower pressures of about 3–4 kbar, during late stages of shear deformation from CO₂-rich fluids as proposed by Krenn et al. [57] for corundum–anorthite assemblages postdating kyanite in desilicated pegmatoid veins within gneisses and amphibolites of the Nestos suture zone, about 4 km south of the Gorgona locality.

In the absence of geochronological data for corundum-bearing assemblages within the Nestos suture zone, it remains difficult to state if they all represent the same metamorphic event, or can be attributed to different P–T conditions corresponding to different ages.

The plumasites from Kinidaros, Naxos contain tourmaline and beryl, in addition to corundum, anorthite and phlogopite, and originate from desilication of leucogranitic pegmatites. For these pegmatites, Matthews et al. [118] reported temperature variations from >700 °C to ~400 °C, based on oxygen isotope fractionation among quartz, tourmaline and garnet, and attributed their formation from anatectic melts during regional high-temperature metamorphism. According to these authors, crystallization of the pegmatitic magmas should initiate under water-undersaturated conditions, but with crystallization of anhydrous minerals and ascent, the magma should evolve to water-saturated conditions at 630 to 640 °C. Thus, some of the higher temperatures (T = 650 °C) given by the isotope thermometry could represent the crystallization at reduced water activity. In addition, Siebenaller [119] used fluid inclusion measurements in tourmaline, garnet and beryl from leucogranite pegmatites from Naxos island, to estimate P–T formation conditions for the pegmatites of between 5 kbar/600 °C and <2 kbar/450 °C, along the exhumation path of leucogranite (Figure 13). The absence of andalusite from the studied corundum-bearing assemblages constrains the lower limit of corundum formation along the retrograde path at about 3 kbar and 550 °C.

Finally, metabauxite occurrences on southern Naxos (Kavalaris Hill) correspond to the thermal dissociation of diaspore and the formation of corundum ($\alpha\text{-AlOOH} \leftrightarrow \text{Al}_2\text{O}_3 + \text{H}_2\text{O}$, Haas [120]), as described by Feenstra and Wunder [73]. The first corundum occurrence in Naxos metabauxites has been recorded as corundum-in isograd (T~420–450 °C and P~6 kbar, [73]). Similarly, the metabauxites from

Ikaria were formed at T in the range 450–550 °C and P ~5–6 kbar [75,77]. According to Iliopoulos [75], the latter correspond to corundum-chloritoid-bearing metabauxites from Naxos island (zones II and III of Feenstra [21]; Figure 13).

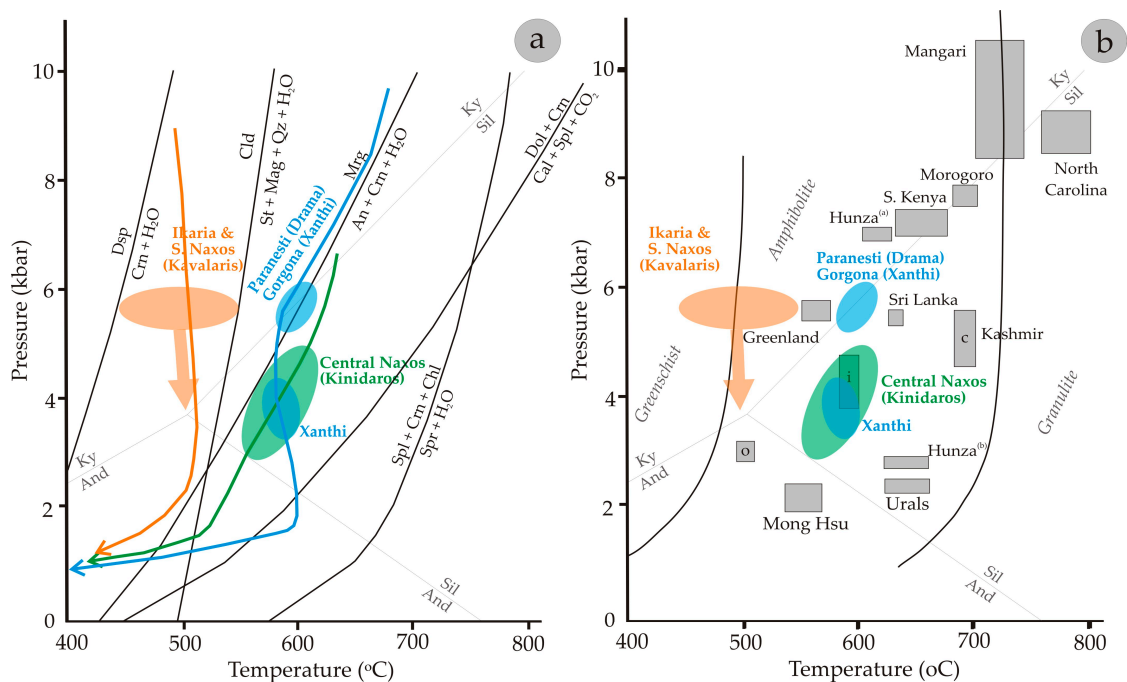


Figure 13. (a) P–T diagram showing mineral equilibria related to the formation of corundum in Greece (modified from Garnier et al. [117]). Upper blue area: Paranesti ruby and Gorgona sapphires ([30] and this study); Lower blue area: Alternative conditions for the Gorgona sapphires (for explanation see text); Orange area: Ikaria and southern Naxos metabauxites. The thick orange arrow indicates possible path for formation of vein-type sapphires from both localities; Green area: Central Naxos plumasites. Blue arrow: P–T–t path of high-grade rocks from the Nestos suture zone (from Krenn et al. [57]); Green arrow: P–T–t path of the tourmaline-garnet-beryl-bearing leucogranite from Naxos island (from Siebenaller [119]); Orange arrow: P–T–t path of the lower limit of metamorphic zone III (which hosts corundum-chloritoid-bearing metabauxites) from Naxos island (from Duchêne et al. [64]). The equilibrium curve “chloritoid + O₂ = staurolite + magnetite + quartz”, which marks the disappearance of chloritoid, defines an upper limit for the studied chloritoid-bearing metabauxites at southern Naxos (Kavalaris) and Ikaria islands is from Feenstra [21]. Abbreviations: An = anorthite; And = andalusite; Cc = calcite; Cld = chloritoid; Clin = clinocllore; Co = corundum; Do = dolomite; Dsp = diasporé; Ky = kyanite; Ma = margarite; Mag = magnetite; Qz = quartz; Sill = sillimanite; Spr = sapphirine; Sp = spinel; St = staurolite; (b) Comparison between the hypothetical P–T conditions for the formation of corundum in Greece and in metamorphic deposits around the world (modified from Giuliani et al. [7], Simonet et al. [3]). Boxes indicate P–T fields of known deposits: North Carolina, Rubies from mafic granulites [121]; Morogoro, corundum-bearing anatexites [122]; Mangari, Southern Kenya, Metasomatic rubies [123–125]; Hunza, rubies in marbles [113]; Sri Lanka, sapphires from granulites [94]; Greenland, metasomatic rubies [126]; Kashmir metasomatic sapphires with three P–T boxes corresponding to the evolution of the fluids in the sapphire crystals from the center (c), to intermediate (i) and outer (o) zones [98]; Urals, rubies in marbles [127], and Mong Hsu, rubies in marbles [128].

However, the studied sapphires from both localities correspond to open space-filling material in extensional fissures and indicate a second, late stage of corundum formation. We interpret this corundum formation to be of metasomatic origin from a low-temperature CO₂-bearing metamorphic fluid, as already proposed for similar sapphire + margarite + tourmaline-filled veins from Naxos island [116]. This is in agreement with the findings of Tropper and Manning [129], who consider corundum-filled hydrofractures in the Naxos metabauxites to be products of retrograde cooling and

decompression, consistent with kinematically late textures. This hypothesis is also supported by the fact that trace element fingerprints of Naxos and Ikaria metabauxite-hosted sapphire suggest magmatic affinities (this study). A hydrothermal origin of diaspore has been reported for the gem-quality diaspore crystals (var. zultanite) occurring in fissures of metabauxites in the İlbir Mountains, SW Turkey [130]. According to the above authors, the diaspore mineralization is caused by hydrothermal remobilization of primary bauxite components into crosscutting structures. Figure 13 displays an evolution (thick orange arrow) towards lower P–T conditions, along the P–T–t retrograde path of the metamorphic zone III (hosting corundum-chloritoid-bearing metabauxites) from Naxos island (according to Duchêne et al. [53]). Since the tectonometamorphic evolution of Ikaria is quite similar to that of Naxos [55,74], this path could probably reflect the formation of the vein-type sapphire assemblages in both Naxos and Ikaria islands.

8.5. Greece: A New Gem Corundum Province?

Greek corundum occurrences display a wide color variation, ranging from deep red, pink, purple, and blue to colorless, with crystal sizes of up to 5 cm. Among the studied occurrences, some corundums from Gorgona/Xanthi and the plumasite-hosted sapphires from Naxos display significant transparency and homogeneity of color and should be further examined for their suitability as potential cut gemstones. The rest of the studied corundums, especially the vivid-colored varieties, could be considered suitable for their use as cabochons. Although gem-quality corundums are considered to be absent in emery deposits [7], the Naxos and especially Ikaria blue sapphires are of gem (cabochon) quality, and are atypical for other metabauxite-hosted corundums. Future exploration is required in order to establish the potential for economic exploitation of the corundum-bearing areas in Greece, pointing towards a new gem corundum province in the world.

We highlight here the enrichment in Be of blue-colorless sapphires from Naxos plumasites, a feature which has only been reported from Ilakaka, Madagascar, Sar-e-Sang, Afganistan and Weldborough, Tasmania, and was attributed to nano-inclusions of unidentified Be-rich phases [131]. The Naxos plumasitic sapphires, as well as those from the Xanthi marbles and Ikaria metabauxites, display very high values in Nb, Ta, W and Sn, much higher than those reported from the above occurrences. A further study of the concentration of these elements and especially of Be in the Greek corundums could be a useful tool for determining their origin [131].

9. Conclusions

Gem corundum in Greece covers in a variety of geological environments located within the Rhodope (Xanthi and Drama areas) and Attico-Cycladic (Naxos and Ikaria islands) tectono-metamorphic units. Pargasite-schist hosted a ruby deposit in the Paranesti/Drama area and marble hosted pink to blue sapphires in the Xanthi area, occurring along the UHP-HP Nestos suture zone. Plumasite-hosted sapphires from Naxos island display a wide color variation (blue to colorless and pink). Deep blue colored sapphires from Naxos and Ikaria islands are hosted within extensional fissures in metabauxite lenses within marbles. Various mineral inclusions in corundums are in equilibrium and/or postdate corundum crystallization, and reflect the surrounding mineralogical assemblages. Included in corundums are: spinel and pargasite (Paranesti), spinel, zircon (Xanthi), margarite, zircon, apatite, diaspore, phlogopite and chlorite (Naxos) and chloritoid, ilmenite, hematite, ulvospinel, rutile and zircon (Ikaria).

The chromophores of the studied corundums show a wide range in concentration and a unique trace element chemistry with variable critical ratios (Fe/Mg, Ga/Mg, Ga/Cr and Fe/Ti). Be, Nb, Sn, Ta and W are anomalously enriched in the plumasite-related sapphires from Naxos.

Based on the geological setting of formation and trace element fingerprints the Paranesti and Xanthi corundum occurrences can be classified as metamorphic s.s hosted mafics/ultramafics and marbles, respectively. Those from central Naxos are of metasomatic origin and are related to desilicated pegmatites crosscutting ultramafic rocks. Finally, blue sapphires from southern Naxos and Ikaria,

hosted in metabauxites, display an atypical magmatic signature indicating a metasomatic origin by fluid-rock interaction. The study of fluid inclusions in corundum showed that they are CO₂-dominant with low density with very small quantities of CH₄ and/or N₂, and water-free. CO₂-rich fluids are probably of metamorphic origin and derived from devolatilization of carbonate formations. Greek corundums are characterized by a wide color variation, homogeneity of the color hues and transparency and could be considered as potential gemstones.

Author Contributions: P.V. and C.M. collected the studied samples. P.V. assisted by C.M., I.G., K.Z., S.M., S.K., K.W., S.H., St.K., J.B., F.Z., V.K., M.T. and G.L. obtained and evaluated the mineralogical data. G.G. and A.F. obtained and evaluated the oxygen isotopic data. V.M. and A.T. conducted the fluid inclusion measurements. P.V., C.M., G.G., V.M., A.T. and S.K. wrote the manuscript.

Funding: This research was partly funded by UNSW MREII Grants and Australian Research Council (ARC) Large Infrastructure and Equipment Funds (LIEF) grant LE0989067 and by LABEX ANR-10-LABX-21—Ressources21, Nancy, France.

Acknowledgments: The authors would like to thank Evangelos Michailidis for his kind help with the SEM in the University of Athens. Two anonymous reviewers and the Editor are especially thanked for their constructive comments that greatly improved the manuscript.

Conflicts of Interest: The authors declare no conflict of interest.

References

1. Garnier, V.; Ohnenstetter, D.; Giuliani, G.; Schwarz, D. Saphirs et rubis. Classification des gisements de corindon. *Règne Minéral* **2004**, *55*, 4–47.
2. Giuliani, G.; Ohnenstetter, D.; Garnier, V.; Fallick, A.E.; Rakotondrazafy, M.; Schwarz, D. The geology and genesis of gem corundum deposits. In *Geology of Gem Deposits*; Mineralogical Association of Canada Short Course Series; Groat, L., Ed.; Mineralogical Association of Canada: Quebec City, QC, Canada, 2007; Volume 37, pp. 23–78.
3. Simonet, C.; Fritsch, E.; Lasnier, B. A classification of gem corundum deposits aimed towards gem exploration. *Ore Geol. Rev.* **2008**, *34*, 127–133. [[CrossRef](#)]
4. Sutherland, F.L.; Schwarz, D.; Jobbins, E.A.; Coenraads, R.R.; Webb, G. Distinctive gem corundum from discrete basalt fields: A comparative study of Barrington, Australia, and west Pailin, Cambodia gem fields. *J. Gemmol.* **1998**, *26*, 65–85. [[CrossRef](#)]
5. Garnier, V.; Giuliani, G.; Ohnenstetter, D.; Schwarz, D.; Kausar, A.B. Les gisements de rubis associés aux marbres de l'Asie centrale et du Sud-est. *Règne Minéral* **2006**, *67*, 17–48.
6. Garnier, V.; Maluski, H.; Giuliani, G.; Ohnenstetter, D.; Schwarz, D. Ar–Ar and U–Pb ages of marble-hosted ruby deposits from central and southeast Asia. *Canad. J. Earth Sci.* **2006**, *43*, 509–532. [[CrossRef](#)]
7. Giuliani, G.; Ohnenstetter, D.; Fallick, A.E.; Groat, L.; Fagan, A.J. The geology and genesis of gem corundum deposits. In *Geology of Gem Deposits*, 2nd ed.; Mineralogical Association of Canada Short Course Series; Groat, L.A., Ed.; Mineralogical Association of Canada: Quebec City, QC, Canada, 2014; Volume 44, pp. 113–134. ISBN 9780921294375.
8. Graham, I.T.; Khin, Z.; Cook, N.J. The genesis of gem deposits. *Ore Geol. Rev.* **2008**, *34*, 1–2. [[CrossRef](#)]
9. Graham, I.; Sutherland, L.; Zaw, K.; Nechaev, V.; Khanchuk, A. Advances in our understanding of the gem corundum deposits of the West Pacific continental margins intraplate basaltic fields. *Ore Geol. Rev.* **2008**, *34*, 200–215. [[CrossRef](#)]
10. Sorokina, E.S.; Karampelas, S.; Nishanbaev, T.R.; Nikandrov, S.N.; Semiannikov, B.S. Sapphire megacrysts in syenite pegmatites from the Ilmen Mountains, South Urals, Russia: New mineralogical data. *Can. Miner.* **2017**, *55*, 823–843. [[CrossRef](#)]
11. Muhlmeister, S.; Fritsch, E.; Shigley, E.J.; Devouard, B.; Laurs, M.B. Separating natural and synthetic rubies on the basis of trace-element chemistry. *Gems Gemol.* **1998**, *34*, 80–101. [[CrossRef](#)]
12. Sutherland, F.L.; Schwarz, D. Origin of gem corundums from basaltic fields. *Aust. Gemmol.* **2001**, *21*, 30–33.
13. Saminpanya, S. Mineralogy and Origin of Gem Corundum Associated with Basalt in Thailand. Ph.D. Thesis, University of Manchester, Manchester, UK, 2000.
14. Giuliani, G.; Fallick, A.E.; Garnier, V.; France-Lanord, C.; Ohnenstetter, D.; Schwarz, D. Oxygen isotope composition as a tracer for the origins of rubies and sapphires. *Geology* **2005**, *33*, 249. [[CrossRef](#)]

15. Abduriyim, A.B.; Kitwaki, H. Determination of the origin of blue sapphire using laser ablation inductively coupled plasma mass spectrometry (LA-ICP-MS). *J. Gemmol.* **2006**, *30*, 23–26. [[CrossRef](#)]
16. Peucat, J.J.; Ruffault, P.; Fritsch, E.; Bouhnik-Le Coz, M.; Simonet, C.; Lasnier, B. Ga/Mg ratio as a new geochemical tool to differentiate magmatic from metamorphic blue sapphires. *Lithos* **2007**, *98*, 261–274. [[CrossRef](#)]
17. Sutherland, F.L.; Duroc-Danner, J.M.; Meffre, S. Age and origin of gem corundum and zircon megacrysts from the Mercaderes–Rio Mayo area, South-west Colombia, South America. *Ore Geol. Rev.* **2008**, *34*, 155–168. [[CrossRef](#)]
18. Papastamatiou, I. The Emery of Naxos. *Geol. Geoph. Res.* **1951**, *1*, 37–68.
19. Andronopoulos, V.; Tsoutrelis, C. Investigation of a Red Corundum Occurrence in Xanthi, Greece. Unpublished Report; Greek Geol. Survey, Athens, Greece. 1964; 8p.
20. Ktenas, C. La géologie de l'île de Nikaria (rédigée des restes de l'auteur par G. Marinos). *Geol. Geoph. Res.* **1969**, *13*, 57–85.
21. Feenstra, A. Metamorphism of Bauxites on Naxos, Greece. Ph.D. Thesis, Instituut voor Aardwetenschappen, Rijksuniversiteit te Utrecht, Utrecht, The Netherlands, 1985.
22. Liati, A. Corundum-and zoisite-bearing marbles in the Rhodope Zone, Xanthi area (N. Greece): Estimation of the fluid phase composition. *Mineral. Petrol.* **1988**, *38*, 53–60. [[CrossRef](#)]
23. Zannas, I. Corundum occurrence at Stirigma-Gorgona area, northern Xanthi. Petrogenesis and color variations. *Miner. Wealth* **1995**, *97*, 9–18.
24. Iliopoulos, I.; Katagas, C. Corundum bearing metabauxites from Ikaria Island (Greece): Mineralogy and geochemistry. In Proceedings of the 10th International Congress of the Geological Society of Greece, Thessaloniki, Greece, 15–17 April 2004; pp. 423–424.
25. Voudouris, P. The minerals of Eastern Macedonia and Western Thrace: Geological framework and environment of formation. *Bull. Geol. Soc. Greece* **2005**, *37*, 62–77.
26. Voudouris, P.; Melfos, V.; Katerinopoulos, A. Precious stones in Greece: Mineralogy and geological environment of formation. Understanding the genesis of ore deposits to meet the demand of the 21st century. In Proceedings of the 12th Quadrennial IAGOD Symposium, Moscow, Russia, 21–24 August 2006.
27. Voudouris, P.; Graham, I.; Melfos, V.; Zaw, K.; Lin, S.; Giuliani, G.; Fallick, A.; Ionescu, M. Gem corundum deposits of Greece: Diversity, chemistry and origins. In Proceedings of the 13th Quadrennial IAGOD Symposium, Adelaide, Australia, 6–9 April 2010; Volume 69, pp. 429–430.
28. Voudouris, P.; Katerinopoulos, A.; Magganis, A. Mineralogical geotopes in Greece: Preservation and promotion of museum specimens of minerals and gemstones. Sofia Initiative “Mineral diversity preservation”. In Proceedings of the IX International Symposium on Mineral Diversity Research and Reservation, Sofia, Bulgaria, 16–18 October 2017; pp. 149–159.
29. Graham, I.; Voudouris, P.; Melfos, V.; Zaw, K.; Meffre, S.; Sutherland, F.; Giuliani, G.; Fallick, A. Gem corundum deposits of Greece: A spectrum of compositions and origins. In Proceedings of the 34th IGC Conference, Brisbane, Australia, 5–10 August 2012.
30. Wang, K.K.; Graham, I.T.; Lay, A.; Harris, S.J.; Cohen, D.R.; Voudouris, P.; Belousova, E.; Giuliani, G.; Fallick, A.E.; Greig, A. The Origin of A New Pargasite-Schist Hosted Ruby Deposit From Paraneisi, Northern Greece. *Can. Mineral.* **2017**, *55*, 535–560. [[CrossRef](#)]
31. Voudouris, P. Hydrothermal corundum, topaz, diaspore and alunite supergroup minerals in the advanced argillic alteration lithocap of the Kassiteres-Sapes porphyry-epithermal system, western Thrace, Greece. *Neues Jahrbuch für Mineralogie Abhandlungen* **2014**, *191*, 117–136. [[CrossRef](#)]
32. Pouchou, J.L.; Pichoir, F. Quantitative analysis of homogeneous or stratified microvolumes applying the model “PAP”. In *Electron Probe Quantitation*; Heinrich, K.F.J., Newbury, D.E., Eds.; Plenum Press: New York, NY, USA, 1991; pp. 31–75.
33. Griffin, W.L.; Powell, W.J.; Pearson, N.J.; O'Reilly, S.Y. GLITTER: Data reduction software for laser ablation ICP-MS. In *Laser Ablation ICP-MS in the Earth Sciences: Current Practices and Outstanding Issues*; Mineralogical Association of Canada Short Course Series; Sylvester, P., Ed.; Mineralogical Association of Canada: Quebec City, QC, Canada, 2008; Volume 40, pp. 308–311.
34. Van Achterbergh, E.; Ryan, C.G.; Jackson, S.E.; Griffin, W.L. Data reduction software for LA-ICP-MS: Appendix. In *Laser Ablation-ICP Mass Spectrometry in the Earth Sciences: Principles and Applications*;

- Mineralogical Association of Canada Short Course Series; Sylvester, P.J., Ed.; Mineralogical Association of Canada: St John's, NL, Canada, 2001; Volume 29, pp. 239–243.
35. Driesner, T.; Heinrich, C.A. The system H_2O -NaCl. I. Correlations for molar volume, enthalpy, and isobaric heat capacity from 0 to 1000 degrees C, 1 to 5000 bar, and 0 to 1 X-NaCl. *Geochim. Cosmochim. Acta* **2007**, *71*, 4880–4901. [[CrossRef](#)]
 36. Sharp, Z.D. In situ laser microprobe techniques for stable isotope analysis. *Chem. Geol.* **1992**, *101*, 3–19. [[CrossRef](#)]
 37. Jolivet, L.; Brun, J.P. Cenozoic geodynamic evolution of the Aegean region. *Int. J. Earth. Sci.* **2010**, *99*, 109–138. [[CrossRef](#)]
 38. Ring, U.; Glodny, J.; Thomson, S. The Hellenic subduction system: High-pressure metamorphism, exhumation, normal faulting and large-scale extension. *Earth Plan. Sci.* **2010**, *38*, 45–76. [[CrossRef](#)]
 39. Jolivet, L.; Faccenna, C.; Huet, B.; Labrousse, L.; Le Pourhiet, L.; Lacombe, O.; Lecomte, E.; Burov, E.; Denèle, Y.; Brun, J.-P.; et al. Aegean tectonics: Strain localization, slab tearing and trench retreat. *Tectonophysics* **2013**, *597*, 1–33. [[CrossRef](#)]
 40. Fytikas, M.; Innocenti, F.; Mannetti, P.; Mazzuoli, R.; Peccerillo, A.; Villari, L. Tertiary to Quaternary evolution of volcanism in the Aegean region. In *The Geological Evolution of the Eastern Mediterranean*; Dixon, J.E., Robertson, A.H.F., Eds.; Geological Society Special Publications: Oxford, UK, 1984; Volume 17, pp. 687–699.
 41. Kydonakis, K.; Brun, J.-P.; Sokoutis, D. North Aegean core complexes, the gravity spreading of a thrust wedge. *J. Geophys. Res. Solid Earth* **2015**, *120*, 595–616. [[CrossRef](#)]
 42. Voudouris, P. *Gemstones and Mineral-Megacrysts in Greece*; University New South Wales: Sydney, Australia, 2010.
 43. Burg, J.-P. Rhodope: From Mesozoic convergence to Cenozoic extension. Review of petro-structural data in the geochronological frame. *J. Virtual Explor.* **2012**, *42*, 1–44. [[CrossRef](#)]
 44. Brun, J.-P.; Sokoutis, D. Kinematics of the Southern Rhodope Core Complex (North Greece). *Int. J. Earth Sci.* **2007**, *96*, 1079–1099. [[CrossRef](#)]
 45. Turpaud, P.; Reischmann, T. Characterization of igneous terranes by zircon dating: Implications for UHP occurrences and suture identification in the Central Rhodope, Northern Greece. *Int. J. Earth Sci.* **2010**, *99*, 567–591. [[CrossRef](#)]
 46. Mposkos, E.; Kostopoulos, D. Diamond, former coesite and supersilicic garnet in metasedimentary rocks from the Greek Rhodope: A new ultrahigh-pressure metamorphic province established. *Earth Plan. Sci. Lett.* **2001**, *192*, 497–506. [[CrossRef](#)]
 47. Liati, A. Identification of repeated Alpine (ultra) highpressure metamorphic events by U-Pb SHRIMP geochronology and REE geochemistry of zircon: The Rhodope zone of Northern Greece. *Contrib. Mineral. Petrol.* **2005**, *150*, 608–630. [[CrossRef](#)]
 48. Gautier, P.; Bosse, V.; Cherneva, Z.; Didier, A.; Gerdjikov, I. Polycyclic alpine orogeny in the Rhodope metamorphic complex: The record in migmatites from the Nestos shear zone (N. Greece). *Bull. Geol. Soc. France* **2017**, *188*, 36. [[CrossRef](#)]
 49. Bonev, N.; Burg, J.-P.; Ivanov, Z. Mesozoic–Tertiary structural evolution of an extensional gneiss dome—The Kesebir–Kardamos dome, eastern Rhodope (Bulgaria–Greece). *Int. J. Earth Sci.* **2006**, *95*, 318–340. [[CrossRef](#)]
 50. Menant, A.; Jolivet, L.; Vrielynck, B. Kinematic reconstructions and magmatic evolution illuminating crustal and mantle dynamics of the eastern Mediterranean region since the late Cretaceous. *Tectonophysics* **2016**, *675*, 103–140. [[CrossRef](#)]
 51. Wüthrich, E. Low Temperature Thermochronology of the Northern Aegean Rhodope Massif. Unpublished Ph.D. Thesis, ETH Zürich, Zürich, Switzerland, 2009.
 52. Melfos, V.; Voudouris, P. Cenozoic metallogeny of Greece and potential for precious, critical and rare metals exploration. *Ore Geol. Rev.* **2017**, *59*, 1030–1057. [[CrossRef](#)]
 53. Duchêne, S.; Aïssa, R.; Vanderhaeghe, O. Pressure-temperature-time evolution of metamorphic rocks from Naxos (Cyclades, Greece): Constraints from thermobarometry and Rb/Sr dating. *Geodin. Acta* **2006**, *19*, 301–321. [[CrossRef](#)]
 54. Ottens, B.; Voudouris, P. *Griechenland: Mineralien-Fundorte-Lagerstätten*; Christian Weise Verlag: München, Germany, 2018; 480p.

55. Beaudoin, A.; Augier, R.; Laurent, V.; Jolivet, L.; Lahfid, A.; Bosse, V.; Arbaret, L.; Rabillard, A.; Menant, A. The Ikaria hightemperature Metamorphic Core Complex (Cyclades, Greece): Geometry, kinematics and thermal structure. *J. Geodesy* **2015**, *92*, 18–41.
56. Papanikolaou, D.; Panagopoulos, G. On the structural style of Southern Rhodope (Greece). *Geol. Balc.* **1981**, *11*, 13–22.
57. Krenn, K.; Bauer, C.; Proyer, A.; Mposkos, E.; Hoinkes, G. Fluid entrapment and reequilibration during subduction and exhumation: A case study from the high-grade Nestos shear zone, Central Rhodope, Greece. *Lithos* **2008**, *104*, 33–53. [\[CrossRef\]](#)
58. Nagel, T.J.; Schmidt, S.; Janák, M.; Froitzheim, N.; Jahn-Awe, S.; Georgiev, N. The exposed base of a collapsing wedge: The Nestos Shear Zone (Rhodope Metamorphic Province, Greece): The Nestos shear zone. *Tectonics* **2011**, *30*. [\[CrossRef\]](#)
59. Bonneau, M. Correlation of the Hellenic nappes in the south-east Aegean and their tectonic reconstruction. *Geol. Soc. Lond. Spec. Publ.* **1984**, *17*, 517–527. [\[CrossRef\]](#)
60. Scheffer, C.; Vanderhaeghe, O.; Lanari, P.; Tarantola, A.; Ponthus, L.; Photiades, A.; France, L. Syn- to post-orogenic exhumation of metamorphic nappes: Structure and thermobarometry of the western Attic-Cycladic metamorphic complex (Lavrion, Greece). *J. Geodyn.* **2016**, *96*, 174–193. [\[CrossRef\]](#)
61. Grasemann, B.; Schneider, D.A.; Stöckli, D.F.; Iglseder, C. Miocene bivergent crustal extension in the Aegean: Evidence from the western Cyclades (Greece). *Lithosphere* **2012**, *4*, 23–39. [\[CrossRef\]](#)
62. Kruckenberg, S.C.; Vanderhaeghe, O.; Ferré, E.C.; Teyssier, C.; Whitney, D.L. Flow of partially molten crust and the internal dynamics of a migmatite dome, Naxos, Greece. *Tectonics* **2011**, *30*. [\[CrossRef\]](#)
63. Laurent, V.; Huet, B.; Labrousse, L.; Jolivet, L.; Monie, P.; Augier, R. Extraneous argon in high-pressure metamorphic rocks: Distribution, origin and transport in the Cycladic Blueschist Unit (Greece). *Lithos* **2017**, *272*, 315–335. [\[CrossRef\]](#)
64. Altherr, R.; Kreuzer, H.; Wendt, I.; Lenz, H.; Wagner, G.A.; Keller, J.; Harre, W.; Höhndorf, A. A late Oligocene/early Miocene high temperature belt in the Attic-Cycladic crystalline complex (SE Pelagonian, Greece). *Geol. Jahrb.* **1982**, *23*, 97–164.
65. Lister, G.S.; Banga, G.; Feenstra, A. Metamorphic core complexes of cordilleran type in the Cyclades, Aegean Sea, Greece. *Geology* **1984**, *12*, 221–225. [\[CrossRef\]](#)
66. Gautier, P.; Brun, J.P. Crustal-scale geometry and kinematics of late-orogenic extension in the central Aegean (Cyclades and Ewia Island). *Tectonophysics* **1994**, *38*, 399–424. [\[CrossRef\]](#)
67. Jansen, J.B.H.; Schuiling, R.D. Metamorphism on Naxos; petrology and geothermal gradients. *Am. J. Sci.* **1976**, *276*, 1225–1253. [\[CrossRef\]](#)
68. Wybrans, J.R.; McDougall, I. Metamorphic evolution of the Attic Cycladic Metamorphic Belt on Naxos (Cyclades, Greece) utilizing $^{40}\text{Ar}/^{39}\text{Ar}$ age spectrum measurements. *J. Metam. Geol.* **1988**, *6*, 571–594. [\[CrossRef\]](#)
69. Buick, I.S.; Holland, T.J.B. The P-T path associated with crustal extension, Naxos, Cyclades, Greece. In *Evolution on Metamorphic Belts*; Daly, J.S., Cliff, R.A., Yardley, B.W.D., Eds.; Geological Society Special Publications: London, UK, 1989; Volume 43, pp. 365–369.
70. Baker, J.; Matthews, A. The stable isotopic evolution of a metamorphic complex, Naxos, Greece. *Contrib. Mineral. Petrol.* **1995**, *120*, 391–403. [\[CrossRef\]](#)
71. Katzir, Y.; Valley, J.W.; Matthews, A.; Spicuzza, M.J. Tracking fluid flow during deep crustal anatexis: Metasomatism of peridotites (Naxos, Greece). *Contrib. Mineral. Petrol.* **2002**, *142*, 700–713. [\[CrossRef\]](#)
72. Andriessen, P.A.M.; Hebedaa, E.H.; Simonb, O.J.; Verschurea, R.H. Tourmaline K/Ar ages compared to other radiometric dating systems in Alpine anatectic leucosomes and metamorphic rocks (Cyclades and southern Spain). *Chem. Geol.* **1991**, *91*, 33–48. [\[CrossRef\]](#)
73. Feenstra, A.; Wunder, B. Dehydration of diaspore to corundum in nature and experiment. *Geology* **2002**, *30*, 119–122. [\[CrossRef\]](#)
74. Laurent, V.; Beaudoin, A.; Jolivet, L.; Arbaret, L.; Augier, R.; Rabillard, A.; Menant, A. Interrelations between extensional shear zones and synkinematic intrusions: The example of Ikaria Island (NE Cyclades, Greece). *Tectonophysics* **2015**, *651–652*, 152–171. [\[CrossRef\]](#)
75. Iliopoulos, I. Petrogenesis of Metamorphic Rocks from Ikaria Island. Ph.D. Thesis, University of Patras, Patra, Greece, 2005.

76. Ring, U. The Geology of Ikaria Island: The Messaria extensional shear zone, granites and the exotic Ikaria nappe. *J. Virtual Explor.* **2007**, *27*, 3.
77. Liati, A.; Skarpelis, N. The metabauxites of Ikaria island, Eastern Aegean, Greece. In Proceedings of the 5th International Symposium on eastern Mediterranean Geology, Thessaloniki, Greece, 14–20 April 2004; pp. 1427–1430.
78. Henry, D.J.; Dutrow, B.L. Compositional zoning and element partitioning in nickeloan tourmaline from metamorphosed karstbauxite from Samos, Greece. *Am. Mineral.* **2001**, *86*, 1130–1142. [[CrossRef](#)]
79. Karantoni, V.D. Gemological Study of Corundum, Variety of Ruby and Sapphire from Greece. Unpublished Master's Thesis, School of Geology, Aristotle University of Thessaloniki, Thessaloniki, Greece, 2018.
80. Bodnar, R.J. Introduction to fluid inclusions. In *Fluid Inclusions: Analysis and Interpretation*; Mineralogical Association of Canada Short Course Series; Samson, I.M., Anderson, A.J., Marshall, D.D., Eds.; Mineralogical Association of Canada: Quebec City, QC, Canada, 2003; Volume 32, pp. 1–8.
81. Giuliani, G.; Fallick, A.; Rakotondrazafy, M.; Ohnenstetter, D.; Andriamamonjy, A.; Ralantoarison, T.; Rakotosamizany, S.; Razanatseho, M.; Offant, Y.; Garnier, V.; et al. Oxygen isotope systematics of gem corundum deposits in Madagascar: Relevance for their geological origin. *Mineral. Depos.* **2007**, *42*, 251–270. [[CrossRef](#)]
82. Giuliani, G.; Fallick, A.E.; Ohnenstetter, D.; Pegre, G. Oxygen isotope composition of sapphire from the French Massif Central: Implications for the origin of gem corundum in basalt fields. *Mineral. Depos.* **2009**, *44*, 221–231. [[CrossRef](#)]
83. Wang, K.K.; Graham, I.T.; Martin, L.; Voudouris, P.; Giuliani, G.; Lay, A.; Harris, S.; Fallick, A.E. Fingerprinting Paranesti rubies through in-situ oxygen isotopes. *Minerals*. (under review).
84. Sutherland, F.L.; Zaw, K.; Meffre, S.; Giuliani, G.; Fallick, A.E.; Graham, I.T.; Webb, G.B. Gem corundum megacrysts from East Australia basalt fields: Trace elements, O isotopes and origins. *Aust. J. Earth Sci.* **2009**, *56*, 1003–1020.
85. Harris, S.J.; Graham, I.T.; Lay, A.; Powell, W.; Belousova, E.; Zappetini, E. Trace element geochemistry and metasomatic origin of alluvial sapphires from the Oros mayo region, Jujuy Province, Northwest Argentina. *Canad. Mineral.* **2017**, *55*, 595–617. [[CrossRef](#)]
86. Sutherland, F.; Zaw, K.; Meffre, S.; Yui, T.-F.; Thu, K. Advances in Trace Element “Fingerprinting” of Gem Corundum, Ruby and Sapphire, Mogoke Area, Myanmar. *Minerals* **2015**, *5*, 61–79. [[CrossRef](#)]
87. Giuliani, G.; Lasnier, B.; Ohnenstetter, D.; Fallick, A.E.; Pégère, G. Les gisements de corindon de France. *Le Règne Minéral* **2010**, *93*, 5–22.
88. Giuliani, G.; Caumon, G.; Rakotozamisany, S.; Ohnenstetter, D.; Rakotondrazafy, M. Classification chimique des corindons par analyse factorielle discriminante: Application à la typologie des gisements de rubis et saphirs. *Rev. Gemmol.* **2014**, *188*, 14–22.
89. Zwaan, J.H.; Buter, E.; Mertz-Kraus, R.; Kane, R.E. Alluvial sapphires from Montana: Inclusions, geochemistry and indications of a metasomatic origin. *Gems Gemmol.* **2015**, *51*, 370–391.
90. Schwarz, D.; Pardieu, V.; Saul, J.M.; Schmetzer, K.; Laus, B.M.; Giuliani, G.; Klemm, L.; Malsy, A.; Erel, E.; Hauzenberger, C.; et al. Rubies and Sapphires from Winza, Central Tanzania. *Gems Gemmol.* **2008**, *44*, 322–347. [[CrossRef](#)]
91. Rakotondrazafy, A.F.M.; Giuliani, G.; Ohnenstetter, D.; Fallick, A.E.; Rakotosamizany, S.; Andriamamonjy, A.; Ralantoarison, T.; Razanatseho, M.; Offant, Y.; Garnier, V.; et al. Gem corundum deposits of Madagascar: A review. *Ore Geol. Rev.* **2008**, *34*, 134–154. [[CrossRef](#)]
92. Pham Van, L.; Hoáng Quang, V.; Garnier, V.; Giuliani, G.; Ohnenstetter, D.; Lhomme, T.; Schwarz, D.; Fallick, A.E.; Dubessy, J.; Phan Trong, T. Gem corundum deposits in Vietnam. *J. Gemmol.* **2004**, *29*, 129–147.
93. Simonet, C.; Paquette, J.L.; Pin, C.; Lasnier, B.; Fritsch, E. The Dusi (Garba Tula) sapphire deposit, Central Kenya—A unique Pan-African corundum-bearing monzonite. *J. Afr. Earth Sci.* **2004**, *38*, 401–410. [[CrossRef](#)]
94. De Maesschalck, A.A.; Oen, I.S. Fluid and mineral inclusions in corundum from gem gravels in Sri Lanka. *Mineral. Mag.* **1989**, *53*, 539–545. [[CrossRef](#)]
95. Giuliani, G.; Dubessy, J.; Banks, D.; Quang, V.H.; Lhomme, T.; Pironon, J.; Garnier, V.; Trong Trinh, P.; Van Long, P.; Ohnenstetter, D.; et al. CO₂-H₂S-COS-S₈-AlO(OH)-bearing fluid inclusions in ruby from marble-hosted deposits in Luc Yen area, North Vietnam. *Chem. Geol.* **2003**, *194*, 167–185. [[CrossRef](#)]
96. Menon, R.D.; Santosh, M.; Yoshida, M. Gemstone mineralization in southern Kerala, India. *J. Geol. Soc. India* **1994**, *44*, 241–252.

97. Rakotondrazafy, A.F.M.; Moine, B.; Cuney, M. Mode of formation of hibonite (CaAl_2O_4) within the U-Th skarns from the granulites of S-E Madagascar. *Contrib. Mineral. Petrol.* **1996**, *123*, 190–201. [\[CrossRef\]](#)
98. Peretti, A.; Mullis, J.; Kündig, R. Die Kaschmir-Saphire und ihr geologisches Erinnerungsvermögen. *Neue Zürcher Zeitung* **1990**, *187*, 59.
99. Srithai, B.; Rankin, A.H. Fluid inclusion characteristics of sapphires from Thailand. In *Mineral Deposits: Processes to Processing. Proceedings of the 5th Biennial SGA Meeting and the 10th Quadrennial IAGOD Symposium, London, UK, 22–25 August 1999*; Stanley, C.J., Ed.; Balkema: Rotterdam, The Netherlands, 1999; pp. 107–110.
100. Touret, J.L.R. Le facies granulite en Norvege meridionale. II. Les inclusions fluids. *Lithos* **1971**, *4*, 423–436. [\[CrossRef\]](#)
101. Newton, R.C.; Smith, J.V.; Windley, B.F. Carbonic metamorphism, granulites and crustal growth. *Nature* **1980**, *288*, 45–50. [\[CrossRef\]](#)
102. Morrison, J.; Valley, J.W. Post-granulite facies fluid infiltration in the Adirondack Mountains. *Geology* **1988**, *16*, 513–516. [\[CrossRef\]](#)
103. Hollister, L.S.; Burruss, R.C.; Henry, D.L.; Hendel, E.M. Physical conditions during uplift of metamorphic terrains, as recorded by fluid inclusions. *Bull. Minéral.* **1979**, *102*, 555–561.
104. Lamb, W.M.; Valley, J.W. Metamorphism of reduced granulites in low- CO_2 vapor-free environment. *Nature* **1984**, *312*, 56–58. [\[CrossRef\]](#)
105. Newton, R.C. Fluids of granulite facies metamorphism. In *Fluid—Rock Interactions during Metamorphism*; Walther, J.V., Wood, B.J., Eds.; Springer: New York, NY, USA, 1986; Volume 5, pp. 36–59.
106. Schuiling, R.D.; Kreulen, R. Are thermal domes heated by CO_2 -rich fluids from the mantle? *Earth Plan. Sci. Lett.* **1979**, *43*, 298–302. [\[CrossRef\]](#)
107. Buick, I.S.; Holland, T.J.B. The nature and distribution of fluids during amphibolite facies metamorphism, Naxos (Greece). *J. Metam. Geol.* **1991**, *9*, 301–314. [\[CrossRef\]](#)
108. Mposkos, E.; Krohe, A.; Baziotis, I. Alpine polyphase metamorphism in metapelites from Sidironero complex (Rhodope domain, NE Greece). In *Proceedings of the XIX CBGA Congress, Thessaloniki, Greece, 23–26 September 2010*; Volume 100, pp. 173–181.
109. Liati, A. Regional Metamorphism and Overprinting Contact Metamorphism of the Rhodope Zone, Near Xanthi (N. Greece): Petrology, Geochemistry, Geochronology. Unpublished Ph.D. Thesis, Technical University of Braunschweig, Braunschweig, Germany, 1986.
110. Storre, B.; Nitsch, K.-H. Zur Stabilität von Margarit im System $\text{CaO-Al}_2\text{O}_3\text{-SiO}_2\text{-H}_2\text{O}$. *Contrib. Mineral. Petrol.* **1974**, *43*, 1–24. [\[CrossRef\]](#)
111. Chatterjee, N. Margarite stability and compatibility relations in the system $\text{CaO-Al}_2\text{O}_3\text{-SiO}_2\text{-H}_2\text{O}$ as a pressure-temperature indicator. *Am. Mineral.* **1976**, *61*, 699–709.
112. Chatterjee, N. The system $\text{CaO-Al}_2\text{O}_3\text{-SiO}_2\text{-H}_2\text{O}$: New phase equilibria data, some calculated phase relations, and their petrological applications. *Contrib. Mineral. Petrol.* **1984**, *88*, 1–13. [\[CrossRef\]](#)
113. Okrusch, M.; Bunch, T.E.; Bank, H. Paragenesis and petrogenesis of a corundum bearing marble at Hunza (Kashmir). *Mineral. Depos.* **1976**, *11*, 278–297. [\[CrossRef\]](#)
114. Haas, H.; Holdaway, M.J. Equilibria in the system $\text{Al}_2\text{O}_3\text{-SiO}_2\text{-H}_2\text{O}$ involving the stability limits of pyrophyllite. *Am. J. Sci.* **1973**, *273*, 449–464. [\[CrossRef\]](#)
115. Seifert, F. Stability of sapphirine: A study of the aluminous part of the system $\text{MgO-Al}_2\text{O}_3\text{-SiO}_2\text{-H}_2\text{O}$. *J. Geol.* **1974**, *82*, 173–204. [\[CrossRef\]](#)
116. Markl, G.; Scharlau, A. Grosse Sapphire, Margarit und Tremolit aus den Smirgel-gruben auf Naxos, Griechenland. *Lapis Mineral. Mag.* **2008**, *33*, 26–35.
117. Garnier, V.; Giuliani, G.; Ohnenstetter, D.; Fallick, A.E.; Dubessy, J.; Banks, D.; Hoang Quang, V.; Lhomme, T.; Maluski, H.; Pêcher, A.; et al. Marble-hosted ruby deposits from Central and Southeast Asia: Towards a new genetic model. *Ore Geol. Rev.* **2008**, *34*, 169–191. [\[CrossRef\]](#)
118. Matthews, A.; Putlitz, B.; Hamiel, Y.; Hervig, R.L. Volatile transport during the crystallization of anatectic melts: Oxygen, boron and hydrogen stable isotope study on the metamorphic complex of Naxos, Greece. *Geochim. Cosmochim. Acta* **2003**, *67*, 3145–3163. [\[CrossRef\]](#)
119. Siebenaller, L. Fluid Circulations during Collapse of an Accretionary Prism: Example of the Naxos Island Metamorphic Core Complex (Cyclades, Greece). Ph.D. Thesis, University of Lorraine, Lorraine, France, 2008.
120. Haas, H. Diaspore-corundum equilibria determined by epitaxis of diaspore on corundum. *Am. Mineral.* **1972**, *57*, 1375–1385.

121. Tenthorey, E.A.; Ryan, J.G.; Snow, E.A. Petrogenesis of sapphirine-bearing metatroctolites from the Buck Creek ultramafic body, southern Appalachians. *J. Metam. Geol.* **1996**, *14*, 103–114.
122. Altherr, R.; Okrusch, M.; Bank, H. Corundum- and kyanite-bearing anatexites from the Precambrian of Tanzania. *Lithos* **1982**, *15*, 191–197. [[CrossRef](#)]
123. Mercier, A.; Debat, P.; Saul, J.M. Exotic origin of the ruby deposits of the Mangari area in SE Kenya. *Ore Geol. Rev.* **1999**, *14*, 83–104. [[CrossRef](#)]
124. Key, R.M.; Ochieng, J.O. The growth of rubies in south-east Kenya. *J. Gemmol.* **1991**, *22*, 484–496. [[CrossRef](#)]
125. Simonet, C. Géologie des Gisements de Saphir et de Rubis. L'exemple de la John Saul Mine, Mangari, Kenya. Ph.D. Thesis, Université de Nantes, Nantes, France, 2000.
126. Garde, A.; Marker, M. Corundum crystals with blue-red color zoning near Kangerdluarssuk, Sukkertoppen district, West Greenland. *Report Gronlands Geologiske Undersokelse* **1988**, *140*, 46–49.
127. Kissin, A.J. Ruby and sapphire from the Southern Ural Mountains, Russia. *Gems Gemmol.* **1994**, *30*, 243–252. [[CrossRef](#)]
128. Peretti, A.; Mullis, J.; Mouawad, F. The role of fluorine in the formation of color zoning in rubies from Mong Hsu, Myanmar (Burma). *J. Gemmol.* **1996**, *25*, 3–19. [[CrossRef](#)]
129. Tropper, P.; Manning, C.E. The solubility of corundum in H₂O at high pressure and temperature and its implications for Al mobility in the deep crust and upper mantle. *Chem. Geol.* **2007**, *240*, 54–60. [[CrossRef](#)]
130. Hatipoğlu, M.; Türk, N.; Chamberlain, S.; Akgün, M. Gem-quality transparent diaspore (zultanite) in bauxite deposits of the İbir Mountains, Menderes Massif, SW Turkey. *Mineral. Depos.* **2010**, *45*, 201–205. [[CrossRef](#)]
131. Pardieu, V. Blue sapphires and Beryllium: An unfinished world quest. *InColor* **2013**, *23*, 36–43.



© 2019 by the authors. Licensee MDPI, Basel, Switzerland. This article is an open access article distributed under the terms and conditions of the Creative Commons Attribution (CC BY) license (<http://creativecommons.org/licenses/by/4.0/>).